A robust line-tracking photogrammetry method for uplift measurements of railway catenary systems in noisy backgrounds

Tengjiao Jiang *, Gunnstein Thomas Frøseth, Anders Rønnquist, Egil Fagerholt

Department of Structural Engineering, Norwegian University of Science and Technology, Rich. Birkelands vei 1A, 7491 Trondheim, Norway

A R T I C L E   I N F O

A B S T R A C T

For electrical railways, contact wires are used to ensure stable and continuous power supply to trains operating on the infrastructure. One crucial design parameter used to control the catenary design is the vertical displacement. The traditional uplift measuring equipment of catenary systems usually requires that targets are installed on the wire, and/or that measurement devices are mounted on the support structure of catenary systems or temporary poles. These methods require track access and substantial time and manpower for installation and measurement. Thus, a portable vision-based tracking system is proposed to enable remote, non-contact and non-target uplift measurements of catenary systems. The challenge in measuring the catenary displacement is to detect a linear rigid body in a noisy background environment with a high sampling frequency. To detect the displacement, a vision-based system with a novel line-tracking technique is used to achieve robust and accurate measurement. The proposed technique is based on a coarse subset and line search and subpixel detection. The line-tracking method is successfully employed for the identification of the important vertical displacements of a contact wire in front of a noisy background. The accuracy, robustness and applicability of the proposed tracking method are demonstrated through numerical experiments, the field uplift measurement of the railway catenary system and the identification of the contact wire in a diverse city environment.

1. Introduction

Railways are essential to most modern societies as they provide a fast, comfortable, energy-efficient, environmentally friendly and reliable mode of transportation for both passengers and goods. Catenary systems are an important part of modern railways as they provide an inexpensive, clean and continuous power supply to trains operating the infrastructure. The state of catenary systems directly affects the operation of railway systems and thereby society as a whole. One way of improving and ensuring the reliability of catenary systems is to monitor the current state to carry out maintenance on the system before serious faults occur [1–4].

Excessive vibration of the catenary system can cause contact loss between the contact wires and the pantograph, which not only interrupts the power supply of trains but also causes arcing and speeds up wear [5–7]. Thus, it is important to mon-

---

* Corresponding author.
  E-mail address: tengjiao.jiang@ntnu.no (T. Jiang).

itor the vibration of contact wires to control the maximum uplift. Moreover, the uplift measurement of the contact wire is one of the most important tests to assess the maximum acceptable speed for new electric vehicles and pantographs [8].

Researchers have developed different methods to measure the displacement response of catenary systems. Laffont et al. [9] used three displacement sensors based on Fiber Bragg Grating (FBG) transducers to monitor the 3D displacement of the contact wire. FBG transducers are mounted on the support structure above the contact wire, and they comprise three mobile rods linked to springs for transmitting the displacement of the contact wire to the transducers. Vázquez et al. [10] used an infrared screen to project the light to pass through the contact wire to a line-scan camera and measure the uplift of the contact wire by the projection in images. Karwowski et al. [11] used laser measuring equipment to measure the uplift of the contact wire. This approach requires a reflective plate installed on the contact wire with a laser displacement meter fixed on the top support structure. Nåvik et al. [12,13] presented a newly developed wireless sensor system consisting of a tri-axis gyroscope, a tri-axial accelerometer and a Digital Motion Processor™. This needs to be mounted on the wires to carry out arbitrary point field measurements of the dynamic behaviour of railway catenary systems.

All of the above methods meet the resolution requirement for measurement, but they have the common problem of requiring track access and equipment installation on the contact wire or the mounting of the measuring devices to the support structure of the catenary system or the temporary poles. This means that these devices require substantial time and manpower to install while disrupting traffic.

For fixed long-term monitoring, these devices are capable of obtaining the required uplift data. However, inspectors still need more portable measurement equipment that can carry out multi-point measurements more conveniently and quickly without disrupting traffic. For field testing, portability, robustness in varying environmental conditions, low power consumption and the possibility of battery operation play a primary role in the choice of the equipment [14]. Thus, it is necessary to develop a complementary portable and robust device for the uplift measurement, convenient and easy to install and use.

Photogrammetry meets these requirements, and equipment can be mounted at a distance from the railway while uplift measurements are carried out in a non-contact way. Park et al. [8] developed a high-speed image measurement system to measure the uplift of the contact wire. This system uses a template matching technique to track a target installed on the contact wire for uplift measurement. Zou et al. [15,16] used a photogrammetric system with an edge detection technique to measure the uplift of a catenary part in a laboratory. Frøseth et al. [17] used a calibrated stereo camera system to measure the uplift of the catenary system in the field by tracking a well-defined target attached to the catenary wire. However, the general problem, which is that the contact wire is challenging to track without the target in front of a noisy background, has not been addressed.

The digital image correlation (DIC) technique [18–21] is the most common image processing technique used to measure full-field displacements. Non-contact measurement by DIC has been carried out in, for example, experimental mechanics [22,23], biomechanics [24,25], civil engineering [26,27], mechanical engineering [28–33], additive manufacturing [34,35] and aerospace engineering [36–38]. However, for the uplift measurement of a railway catenary wire in front of a noisy background, DIC does not work very well due to loss of correlation caused by the noisy background. The current paper presents a vision-based tracking system for remote, non-contact and non-target uplift measurement of the contact wire. The challenge to detect a linear rigid body motion in front of a noisy background environment with subpixel accuracy has been addressed by a novel line-tracking technique. In this work, components of the vision-based tracking system are first described. Next, the principles of the line-tracking technique are described in detail. The proposed technique uses two different subpixel detection methods to handle different working conditions to increase applicability. Finally, the accuracy, robustness and applicability of the line-tracking method are demonstrated through numerical experiments, the field uplift measurement of the railway catenary system and the identification of the contact wire in a diverse city environment. Open-source code of the proposed line-tracking technique has been published in [47]. The technique can also be modified to be applied to identify and track linear objects in other fields, such as lane line detection and tracking [39], linear welded seams detection [40], or power line detection and inspection [41,42].

2. Tracking problem in front of a noisy background

The railway catenary system is a power supply system, the task of which is to continuously transmit electricity through the pantograph-catenary interaction to power trains. The main structural parts of the catenary system are a contact wire, a messenger wire and droppers (occasionally also including a stitch wire) [12], all shown in Fig. 1. The contact wire moves on the panhead from side to side as the train goes along the track, as shown in Fig. 2. If there is an additional small horizontal motion from the vibration of the wire, this will be negligible for the interaction between the pantograph and contact wire. Therefore, the uplift measurement is more important than the horizontal displacement measurement.

The vision-based tracking system, used to perform the measurements, is set next to the railway and is perpendicular to the contact wire in the horizontal plane ($\beta = 0$). A schematic overview of the uplift measurement and the vision-based tracking system is given in Fig. 3. The system consists of a high-speed area scan camera (Basler ACA2000-165 μm), a fixed-focal optical lens (the focal length of the lens can be changed according to the actual condition), a trigger, a laptop and a laser range finder (Leica DISTO™ D8). The entire system is powered by the laptop battery/power supply. A laser range finder is
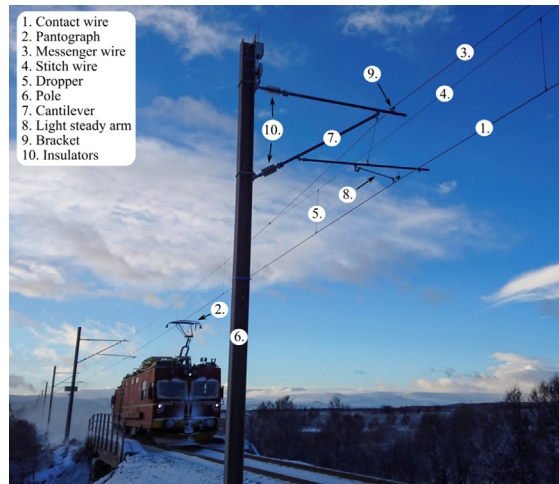
Fig. 1. Main structural components of a railway catenary system. Photo: Petter Nåvik/NTNU.

used to measure the horizontal distance L_H from the system to the catenary wire and the tilt angle α of the optical axis, which are important parameters for camera calibration. The tilt angle α is small but usually not equal to 0 in the field measurement.

Under ideal conditions, the background of the image taken by the camera is uniform, as shown in Fig. 4(a). In general, however, the background of the image consists of a nonuniform or noisy background that makes it challenging to identify and track the contact wire, as shown in Fig. 4(b). In simple approaches to track the contact wire in front of a noisy background, the tracking algorithm may lose the tracking or mistake, for instance, a tree branch for the contact wire and disrupt the performance of the measurement system. Therefore, it is necessary to impose restrictions on the search for the contact wire tracking. A novel line-tracking technique has been proposed to track the contact wire in front of a noisy background while avoiding the above issue.

3. Line-tracking technique for tracking contact wire in a noisy background

For the purpose of successfully tracking the contact wire in a noisy background, a novel line-tracking technique is proposed. There are three main features of this specific tracking problem that will be used to establish a robust line-tracking algorithm.

- A. The contact wire is assumed to be a straight line in all images.
- B. The contact wire has a similar intensity magnitude along the wire in monochrome images, and there is generally a sufficient intensity difference between the wire and the background.
- C. The contact wire crosses the image from left to right.

Regarding point A, the most common span lengths of contact wires range from 40 to 60 m, where the contact wire is pre-stressed and suspended by droppers. Vibration measurements require only a short segment (1 m or shorter), rendering the final cropped segment of the contact wire in the images a straight line. Regarding point B, the similar intensity magnitude along the wire in monochrome images means that the intensity value of the contact wire in the images is usually stable, and parts along the wire stay at similar intensity values. For 8-bit images, the intensity ranges from 0 to 255, with 0 meaning black, and 255 meaning white. For most background scenes, there is generally a sufficient intensity difference between the background and the contact wire. For scenes where this is not the case, e.g., tunnel or metro railway systems, artificial
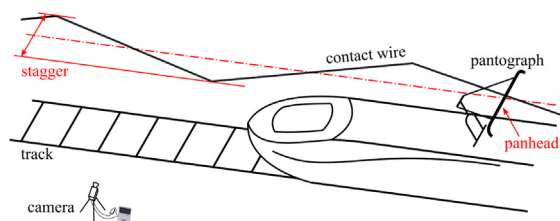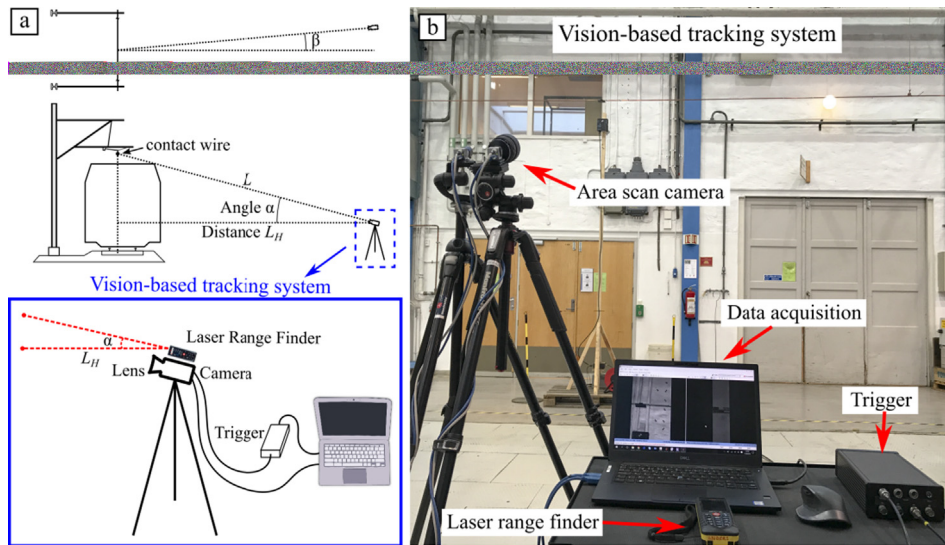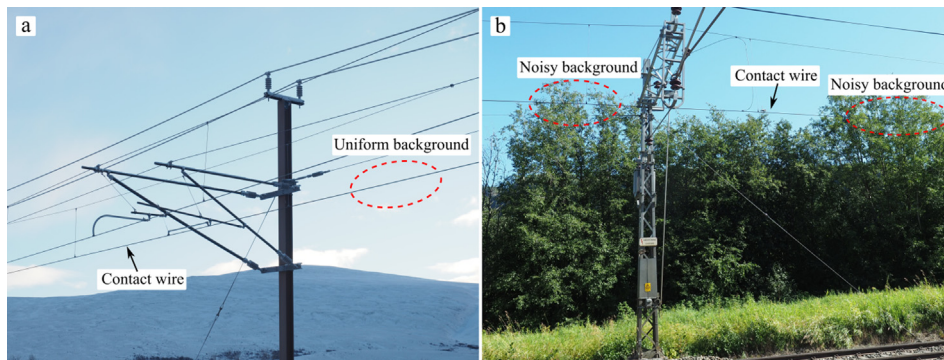

Fig. 2. Stagger of the contact wire.

Fig. 3. The main components of the vision-based tracking system. (a) A schematic overview of the uplift measurement of a railway catenary system. (b) The vision-based tracking system.

Fig. 4. Different backgrounds for the contact wire tracking. (a) Uniform background. (b) Noisy background. Photo: Petter Nåvik/NTNU.

lighting may be necessary to successfully track the contact wire. Finally, regarding point C, every measurement setup aims to have the contact wire centred and close to horizontal in the images. Thus, the contact wire always crosses the image from left to right. In certain situations, the camera view is momentarily obstructed during measurements. In these cases, line tracking may still be possible if horizontal sections of the image that are not obstructed are cropped from the original image and used in the line-tracking algorithm.

Based on these three main configuration points, an algorithm for detecting and tracking linear objects in front of a noisy background is proposed. The line-tracking algorithm consists of a coarse search followed by subpixel detection. The coarse search aims to identify the linear objects in noisy background environments. Subsequently, the subpixel detection method aims to find the position of the contact wires more accurately. The workflow of the tracking algorithm is shown in Fig. 5.

3.1. Coarse search

The coarse search includes two parts: a vertical subset search followed by a line search, where the detailed flow is shown in Fig. 5. The image coordinate system is defined with the origin in the upper-left corner of the image. The intensity values in the image are defined by $f(x, y)$ where x is the column number and y is the row number.

The subset is a square region that contains a part of the image. The vertical subset search aims to identify candidate end-points of the wire in the image. This is carried out by a "sliding" region-of-interest (ROI) or subset moving in the vertical direction at the left and right sides of the image. For each vertical position, the maximum intensity value g_e inside the subset is found. If g_e is less than a threshold G_{et}, the subset is considered an endpoint candidate of the contact wire. The intensity threshold G_{et} can be taken as smaller than the background intensity and larger than the contact wire intensity, usually taken as the average value of both. The idea, here, is that a good candidate subset should be covered entirely by the contact wire.
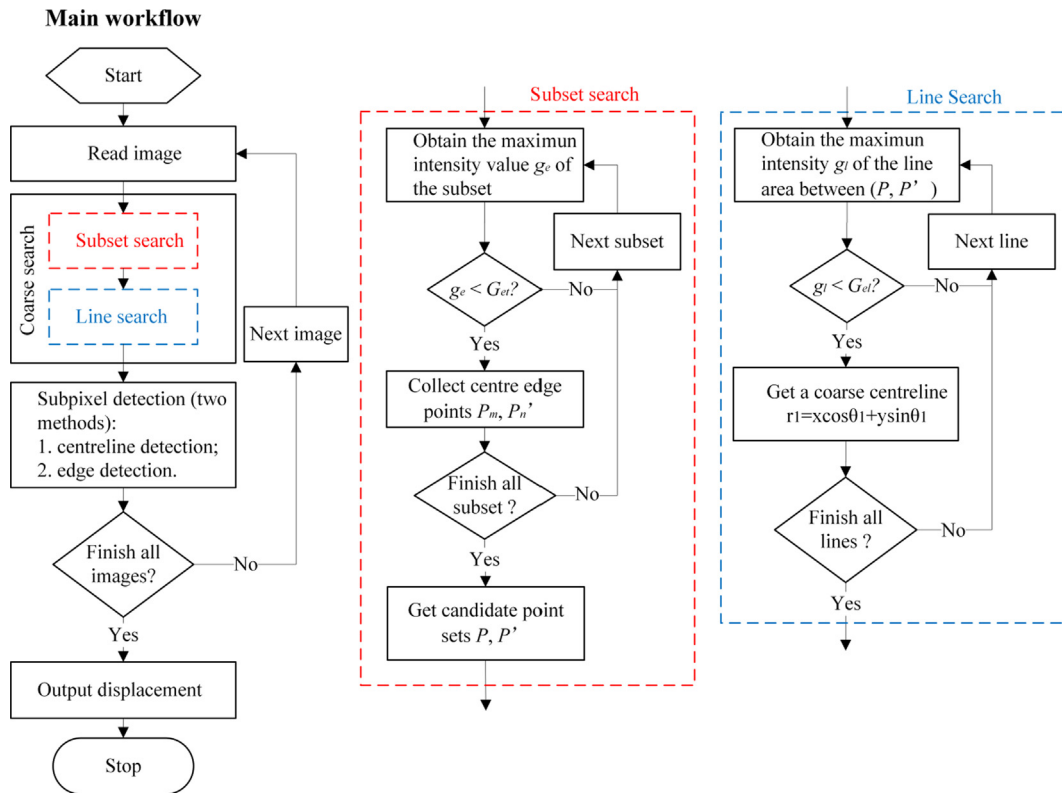
Fig. 5. The main workflow of the line-tracking algorithm, including the coarse search method and subpixel detection method.

Thus, a subset size smaller than the diameter of the contact wire should be chosen. Initially, this procedure is carried out both on the left and right sides of the image.

In Fig. 6, subset A_1 meets the requirement ($g_e < G_{et}$), and the centre edge point a_1 of the subset is obtained as a candidate point. Similarly, b_1 is obtained from subset B_1. Because the subset size is selected to be significantly smaller than the contact wire diameter, several neighbouring candidate points will be obtained as well (illustrated by a_1 to a_5 in Fig. 6). Here, the centre point P_m of a_1 to a_5 is calculated and chosen to represent a_1 to a_5 as a single candidate point.

If one of these vertical searches fails to find the candidate points (either at the left or the right side of the image), the algorithm steps a few pixels horizontally towards the centre of the image and carries out a new vertical search. This is done until at least one qualified candidate point is found both for the left and right sides of the image. The vertical search may, however, result in multiple candidate point sets P (left) and P' (right), as illustrated in Fig. 7.

The line search aims to reduce the sets of candidate points P and P' to only contain endpoints of the wire. For all combinations of P-P', the maximum intensity value g_l along the line between points in P and P' is found. The lines are illustrated in Fig. 7. As discussed in conditions A and B, the contact wire is assumed to be a straight line in all images with a similar intensity magnitude along the wire. Thus, the maximum intensity value of the line area of the "true" contact wire stays at a low intensity range. For a noisy background, as is often the case in most working conditions, there are always higher intensity values in the search line area caused by the background sky, leaves, etc.

As shown in Fig. 6, every point on the search line $r = x\cos\theta + y\sin\theta$ is represented as $P_l (x_l, y_l)$. $r = x\cos\theta + y\sin\theta$ is the linear expression used in the Hough transform [43], shown in Fig. 7, where r is the distance from the origin O to the closest point on the straight line, θ is the angle between the X-axis and the line connecting the origin O with the closest point, and the coordinate system is still the original XOY coordinate system.

The search line area between candidate points P_m and P'_n is set by building search windows (red dashed rectangle in Fig. 6) centred on $P_l (x_l, y_l)$ along the search line. The search window aims to obtain the maximum intensity value g_l of this line area and then compared with the intensity threshold G_{el}. If g_l is smaller than G_{el}, this line is considered the approximate wire position, and the combination (P_m, P'_n) and the coefficients (r_1, θ_1) of the coarse centreline $r_1 = x\cos\theta_1 + y\sin\theta_1$ are obtained. The height of the search window is set to be a value smaller than the diameter of the contact wire to reduce the probability of detection error. In the example in Fig. 6, the height of the search window (red dashed rectangle) is set to 7 pixels, while the diameter of the contact wire is approximately 9 pixels.

The line function $r = x\cos\theta + y\sin\theta$ is used instead of $y = a + bx$ to avoid the problem of calculating the slope when the line is vertical. In this study, the contact wire is assumed to be positioned horizontally in the image. However, by choosing a more
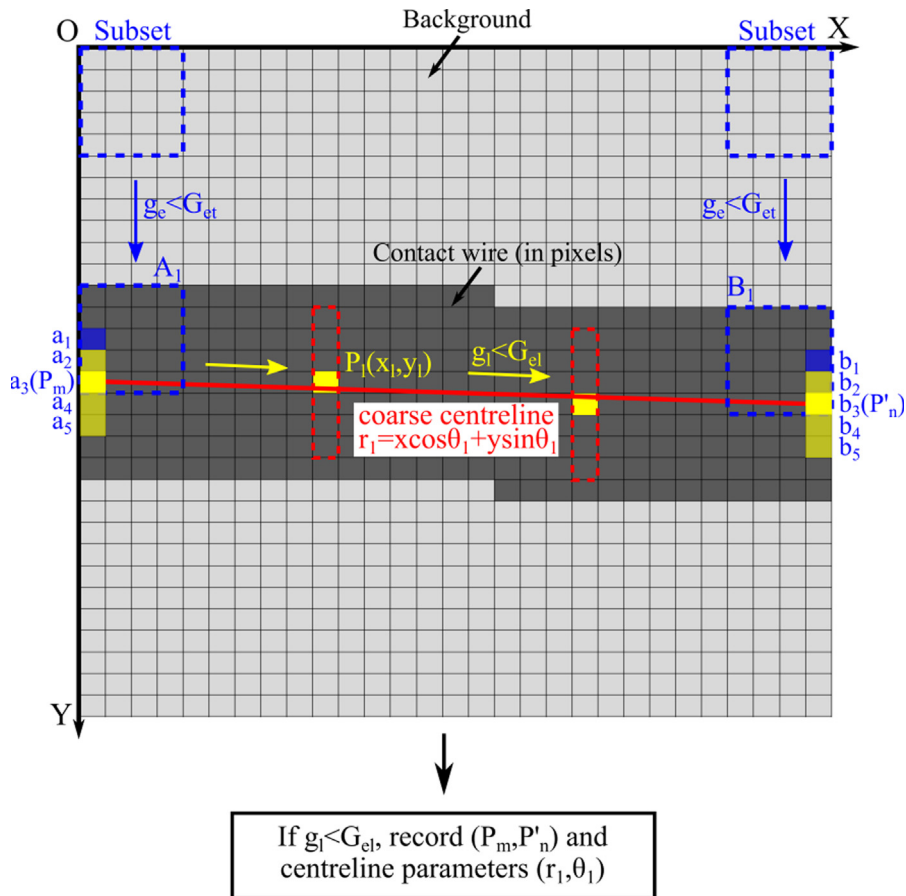
Fig. 6. The sketch of the coarse search method, including the subset search and line search.
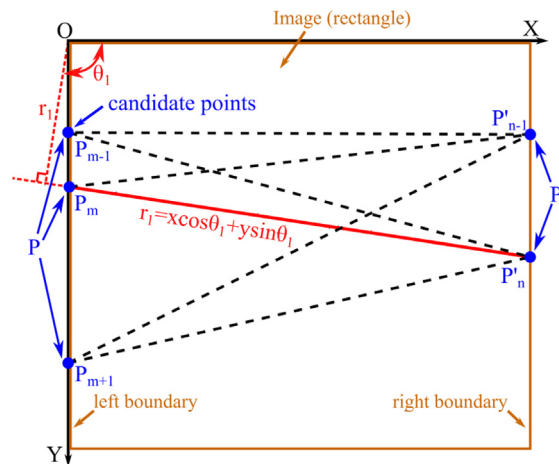

Fig. 7. Line search.

general mathematical line formulation, the algorithm can handle lines with arbitrary rotation, which may be encountered when this line-tracking algorithm is applied in other fields.

In conclusion, if the maximum intensity values g_e and g_l for the vertical subset search and the line search meet the requirement of Eq. (1), the object is considered to be one of the target linear objects.

$$\begin{cases} g_e < G_{et} \\ g_l < G_{el} \end{cases} \tag{1}$$

3.2. Subpixel detection

In the coarse search described in the previous section, all points were represented as integer pixel positions. However, the detection of the contact wire can be improved by applying subpixel detection methods. In this study, two different approaches for subpixel detection of the contact wire were applied, i.e., a centreline detection algorithm, and an edge detection algorithm.

Depending on the specific working conditions, one of these two detection methods can be selected to increase the applicability of the proposed algorithm. For example, when intense sunlight shines at the top of the contact wire, the dark areas of the contact wire become smaller, and the centreline detection method may not work very well. However, there can still be sufficient intensity difference between the lower part of the wire and the background, enabling the edge detection method. Moreover, when the background is very noisy and it is challenging to detect the edge of the contact wire, the centreline detection method can be used to track the contact wire. The reason for proposing two different detection methods is to handle different working conditions.

3.2.1. Method 1: Subpixel centreline detection

The coarse search obtains the locations of the contact wire endpoints at integer pixel positions. The subpixel centreline algorithm then carries out intensity value interpolation in local areas centred on these endpoints.

The method is similar to the previously described vertical subset search. However, here, the intensity values of the subsets are calculated at subpixel positions using bicubic interpolation. The main idea is to use bicubic interpolation to approximate the upper and lower edges of the contact wire to calculate the centre points of the target area accurately. The main calculation process is as follows:

    A. Find the vertical search scope (see Fig. 8). The search scopes are centred on the endpoints and should be large enough to contain both the upper and lower edges of the wire.

    B. A subpixel subset is defined with a suitable size (red dashed rectangles in Fig. 8). The subpixel subset should be entirely covered by the wire, so the subset size should be at least smaller than the diameter of the wire. The intensity values of the subset unit are interpolated using bicubic interpolation. The subpixel subset is used to search both the left and right search scopes vertically. For the sake of clarity, a vertical step interval of 0.5 pixels was applied in Fig. 8. By following a similar procedure as presented in the coarse subset method, the upper and lower edges of the wire are found with 0.5-pixel resolution. Here, the same criteria as in the coarse subset method were applied, i.e., if the maximum intensity value g_e within a subset at a given position is less than the threshold G_{et}, the subset is considered to be entirely covered by the wire. The centre edge point of this subset is obtained as a candidate point (yellow rectangles in Fig. 8).

    C. When all candidate points are found in both the left and right search scopes, these candidate points are usually neighbouring and continuous (yellow bands in Fig. 8). Therefore, the centre point of the yellow band is chosen to represent these candidate points as a single candidate point for this region. Here, the centre points $P_{centre1}$ (x_{ave1}, y_{ave1}) and $P_{centre2}$ (x_{ave2}, y_{ave2}) are shown in Fig. 8 (red rectangles). A line between these two centre points is the centreline $r_2 = x\cos\theta_2 +- y\sin\theta_2$. Finally, a point on this centreline can be selected as a tracking point P_{track} (x_k, y_P). x_k is a constant user-defined x coordinate, and the tracking point P_{track} (x_k, y_P) satisfies $r_2 = x_k \cos\theta_2 + y_P \sin\theta_2$.

Note that the uplift measurement of the contact wire needs to measure the displacement in the y-direction only, so the x coordinate of the tracking point P_{track} is set as a fixed value x_k in Fig. 8. The centreline may not be the actual centreline of the cross-section of the contact wire because the apparent line is affected by the brightness of the light irradiating on the contact wire. To be more precise, the apparent line is the centreline of the partial area of the contact wire, the intensity value of which is less than the threshold G_{et}. This phenomenon does not affect the detection of the contact wire because the natural light usually does not change frequently, so the centreline detection can always track the same position of the contact wire.

3.2.2. Method 2: Subpixel edge detection

In contrast to centreline detection, subpixel edge detection focuses on tracking an edge point in an edge tracking window. The edge is one of the most basic and key features of an image, and edge detection is a main feature extraction method of image analysis. Since the contact wire in the image is considered a straight line, the edge can also be considered a straight line, represented by the equation $y = a + bx$, where the coordinate system is still defined with the origin in the upper-left corner of the image. The subpixel edge detection method based on the partial area effect, introduced in [44], is used in this part.

If an edge passes through the pixel point (i, j), mentioned in [44,45], the intensity value of this pixel is considered as follows:
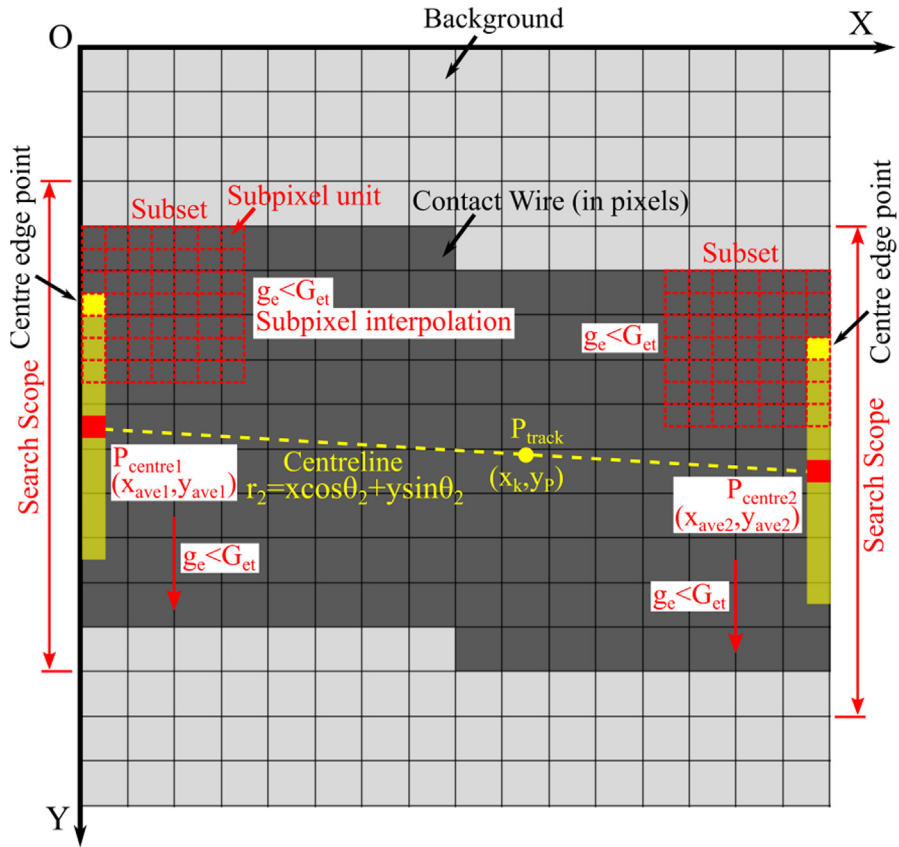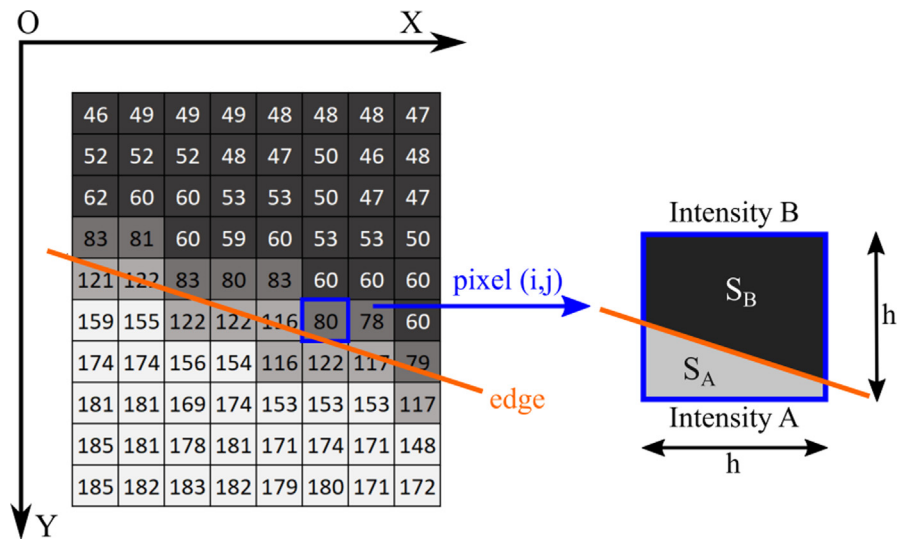
Fig. 8. Subpixel centreline detection.

Fig. 9. Origin of the intensity value of the pixel (i, j).

$$f(i,j) = \frac{AS_A + BS_B}{h^2} \tag{2}$$

where $f(i, j)$ is the intensity value of the pixel point (i, j); A and B are intensity values at both sides of the edge, S_A and S_B are the areas covered by the two intensity values A and B, respectively, in the pixel point (i, j), and h is the side length of the pixel, usually taken as 1, see Fig. 9.

Due to $h^2 = S_A + S_B$,

$$f(i,j) = B + \frac{A - B}{h^2} S_A \tag{3}$$

Before starting the edge detection, to reduce the influence of the noisy background, the original image is smoothed using a 3 × 3 Gaussian smoothing kernel. Gaussian smoothing is used to blur the image by attenuating high-frequency measurement noise and suppressing details in the background. This is achieved by image convolution. The size 3 × 3 means that the 3 × 3-pixel points are convoluted by using the 3 × 3 Gaussian smoothing kernel, and the obtained intensity value is assigned to the central pixel point. The 2D function of an isotropic Gaussian is as follows:

$$G(x, y) = \frac{1}{2\pi\sigma^2} e^{-\frac{x^2+y^2}{2\sigma^2}} \tag{4}$$

Eq. (4) is used to calculate the weight of each point of a 3 × 3 Gaussian smoothing kernel, and the sum of all weights should be equal to 1. In general, larger σ means more smoothing, i.e., more details are removed in the image. σ should not be too big because it smears the edge of the contact wire and makes it non-distinct, but it should be big enough such that it attenuates measurement noise and suppresses details in the background sufficiently. In practical applications presented in work for this article, a kernel of size 3 × 3 with σ = 1.5 has shown to give the appropriate level of smoothing and has been used in all results presented in the article.

Fig. 10 shows the weight distribution of the 3 × 3 Gaussian smoothing kernel with σ = 1.5. The red dot indicates the weight value of the corresponding point of the pixel on the Gaussian smoothing surface. At the bottom of the coordinate is the 3 × 3-pixel convolution region. Red means significant influence on the intensity value of the central convoluted pixel, and blue means little influence. The closer to the central pixel, the higher the weight coefficient and the greater the influence. The reason why the kernel size is 3 × 3 is that the edge detection area is small, and the large kernel will affect the detail quality of the image. To retain the edge intensity gradient, the minimum kernel size is selected.

In the previous coarse search, the point $P_k (x_k, y_k)$ was obtained from the coarse centreline (red line as shown in Fig. 11, where P_k satisfies $r_1 = x_k\cos\theta_1 + y_k\sin\theta_1$. To improve the smoothing efficiency, the smoothing area can be a small area centred on point $P_k (x_k, y_k)$ and at least larger than the edge detection area. The edge detection area contains the tracking window and the area for calculating intensities A and B. After smoothing, a P × 3 tracking window (purple rectangle) with the top edge centred on point $P_k (x_k, y_k)$ is built to detect the subpixel edge. The reason for choosing the lower edge of the contact wire to identify is that the lower edge is usually not illuminated by light, so this edge has a stronger intensity contrast with the background and is easier to identify. The main calculation process is as follows:

First, according to Eq. (3), the sum of the intensity values of every column inside the tracking window is calculated:

$$
\begin{aligned}
L &= \sum_{n=y_k}^{n=y_k+P-1} f(x_k - 1, n) = PB + (A - B)S_L \\
M &= \sum_{n=y_k}^{n=y_k+P-1} f(x_k, n) = PB + (A - B)S_M \\
R &= \sum_{n=y_k}^{n=y_k+P-1} f(x_k + 1, n) = PB + (A - B)S_R
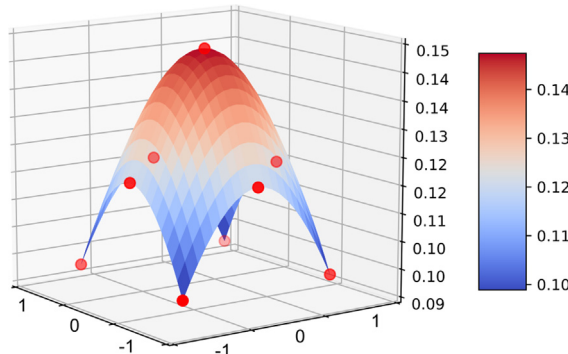\end{aligned}
\tag{5}
$$

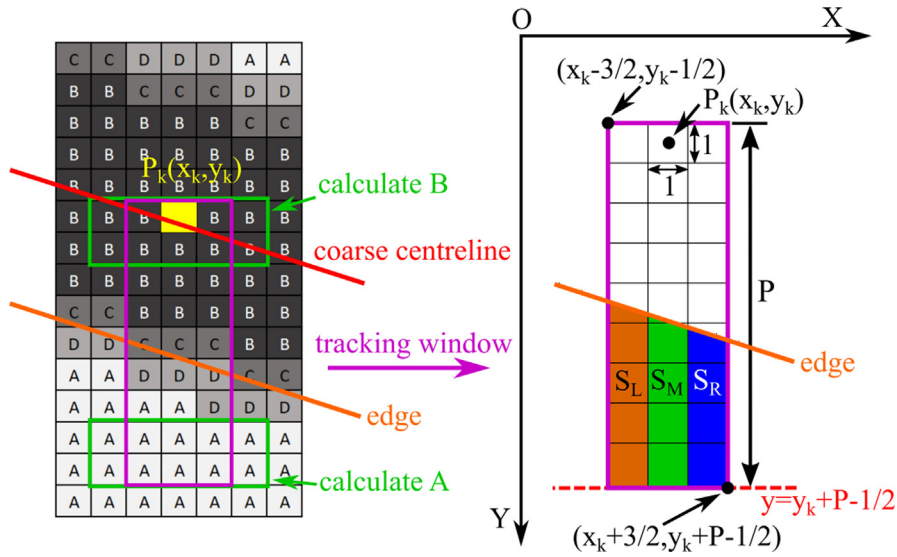**Fig. 10.** 3 × 3 Gaussian smoothing kernel.

Fig. 11. Subpixel edge detection.

where L, M, and R are the sums of intensity values of the left, middle and right columns of the tracking window, respectively. P, the height of the tracking window, can be taken as the diameter of the contact wire with integer pixels. In this way, the edge line can be located in the centre of the tracking window. The side length h is taken as 1. S_L, S_M, and S_R are the areas of each column under the edge, as shown in Fig. 11, and the expressions are as follows:

$$S_L = \int_{x_k-3/2}^{x_k-1/2} [(y_k + P - 1/2) - (a + bx)] \cdot dx = y_k - bx_k + P - a + b - 1/2$$

$$S_M = \int_{x_k-1/2}^{x_k+1/2} [(y_k + P - 1/2) - (a + bx)] \cdot dx = y_k - bx_k + P - a - 1/2 \tag{6}$$

$$S_R = \int_{x_k+1/2}^{x_k+3/2} [(y_k + P - 1/2) - (a + bx)] \cdot dx = y_k - bx_k + P - a - b - 1/2$$

Then, combining (5) and (6), we can obtain the parameters (a, b) of the edge line:

$$a = y_k - bx_k + P - \frac{1}{2} - \frac{M-PB}{A-B}$$
$$b = \frac{L-R}{2(A-B)} \tag{7}$$

One of the most important factors affecting the accuracy of subpixel edge detection is the calculation of A and B, which are the average intensity values of the background and the contact wire, separately. When the background has smooth luminosity gradients, to reduce the influence of noisy pixels on the overall calculation accuracy, it is preferred to calculate the average intensity values in a large area of the background and the contact wire. Thus, A and B can be calculated separately by adding the intensity values of 2 rows and 5 columns of pixels (or even larger) at the bottom of the tracking window (entirely covered by the background) and at the top (entirely covered by the wire), see the green rectangle in Fig. 11. The values can be expressed as:

$$A = \frac{1}{10} \sum_{m=-2}^{m=2} \sum_{n=-1}^{n=0} f(x_k + m, y_k + P - 1 + n)$$

$$B = \frac{1}{10} \sum_{m=-2}^{m=2} \sum_{n=0}^{n=1} f(x_k + m, y_k + n) \tag{8}$$

However, when the background has sharp luminosity gradients, it is preferred to calculate the average intensity values of 2 rows and 3 columns of pixels at the bottom and top inside the tracking window.

When the edge line $y = a + bx$ has been obtained, the edge point $P_e(x_k, a + bx_k)$ can be selected as the tracking point to track the displacement response of the contact wire, while x_k is also the same user-defined constant x coordinate.

Multiple tracking windows may increase measurement accuracy and increase robustness in cases where a single window fails due to, e.g., unfavourable background. In addition, the edge detection requires the edge to cross the tracking window to calculate the integration function Eq. (6), so when the edge slope b is too large, the coordinate system should be changed to

avoid the edge being close to vertical. However, for contact wire detection, this is not a problem since the contact wire is usually close to horizontal.

The edge detection method in [44] uses traditional derivative masks to compute the intensity gradient for every pixel to determine the location of edge pixels. This edge detection method is adapted to detect the contact wire by using the proposed coarse search method to find the wire edge. This change makes the edge detection more efficient for the specific case of identifying a contact wire from noisy backgrounds.

4. Numerical experiment validation

Four sets of numerical experiments, i.e., analysis on synthetically generated image sequences, were conducted to test the performance of the proposed line-tracking method. The first numerical experiment tests the accuracy and stability of the proposed method by tracking the contact wire with precisely controlled motions in front of a noisy background. The algorithm application is introduced in detail in this experiment. The second numerical experiment tests the minimum recognizable diameter of the contact wire in the image and the effect of the diameter change of the contact wire on tracking accuracy. The third numerical experiment adds Gaussian noise to the image to test the noise sensitivity of the tracking method. The fourth experiment simulated the illuminated wire and background to test the performance of the line-tracking method under different light intensity situations.

4.1. Tracking accuracy with a noisy background

To demonstrate the accuracy and robustness of the proposed method with a noisy background, numerical experiments with different subpixel moving distances of the contact wire were conducted. An image (540×778 pixels) with many tree branches and leaves was used as a noisy background. To accurately control the subpixel movement of the contact wire, a straight black line was used as the contact wire, as shown in Fig. 12. According to the general measurement, the 12-mm diameter of the contact wire was approximately 18.79 pixels in the image with the horizontal distance of 12 m and the focal length of the lens of 105 mm. To increase the difficulty of tracking, the diameter of the introduced black line was reduced to 5 pixels to closely resemble the size of the tree branch.

The contact wire was moved downwards with a displacement interval of 0.1 pixels, meaning that each time a 0.1-pixel movement was completed, a new image with a new contact wire position was saved. The 0.1-pixel displacement was achieved by upscaling the background image by a factor of 10 using bicubic interpolation, drawing the line with the displacement of 1 pixel and finally downscaling the image by a factor 10. With the displacement ranging from 0 to 8.0 pixels, a sequence of 81 images was generated and then processed separately by three different subpixel detection methods, i.e., centreline detection, edge detection with and without Gaussian smoothing.
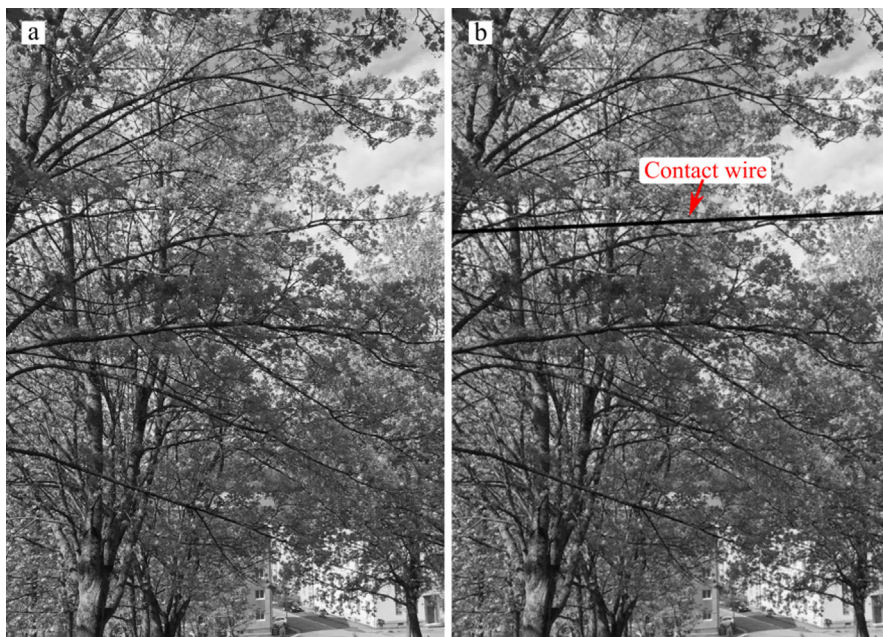

Fig. 12. Noisy background image. (a) Original image. (b) A black line is used as a contact wire in front of the noisy background. Photo: Tengjiao Jiang/NTNU.
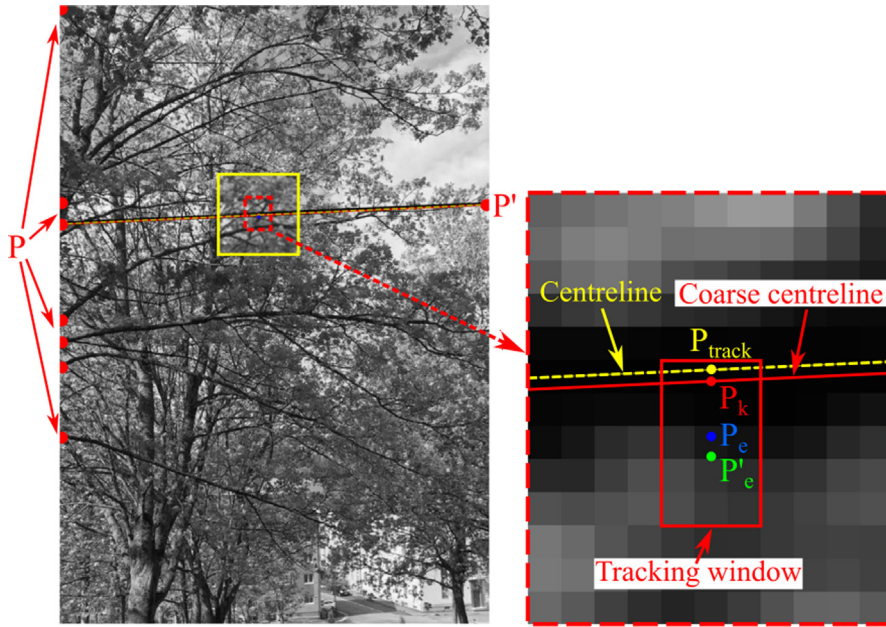
Fig. 13. Contact wire detection results.

The detection result of the contact wire in front of the noisy background is shown in Fig. 13. The left and right boundaries of the image are set as the coarse search columns. After the subset search, the candidate point sets P and P' for the left and right boundaries are obtained, respectively. P has seven candidate points, and P' has one candidate point, where the maximum intensity value g_e is less than the intensity threshold G_{et}. Then, after a line search, the contact wire is successfully identified, and the coarse centreline (solid red line) and point P_k (red point) are obtained, as shown in Fig. 13.

Next, the three detection methods process the image separately. For centreline detection, the algorithm detects search scopes at both ends of the contact wire. After the search, the centreline (yellow dashed line) and the tracking point P_{track} (yellow point) can be obtained, as shown in Fig. 13.

For edge detection without Gaussian smoothing, the 5×3 tracking window (red rectangle in Fig. 13) is built with the pixel point P_k as the centre of the top edge. After edge detection in the tracking window, the edge tracking point P'_e (green point) can be obtained. For edge detection with Gaussian smoothing, first, the algorithm needs to smooth the edge detection area. The edge detection area covers the tracking window and the area of calculating intensities A and B; therefore, the smoothing area should be at least larger than the edge detection area. The Gaussian smoothing kernel with size 3×3 and $\sigma = 1.5$ has been used in all results presented in the article, and the smoothing effect is shown in Fig. 14. In this case, to show the smoothing result more clearly, the size of the smoothing area is selected as 60×60 pixels, shown as the yellow
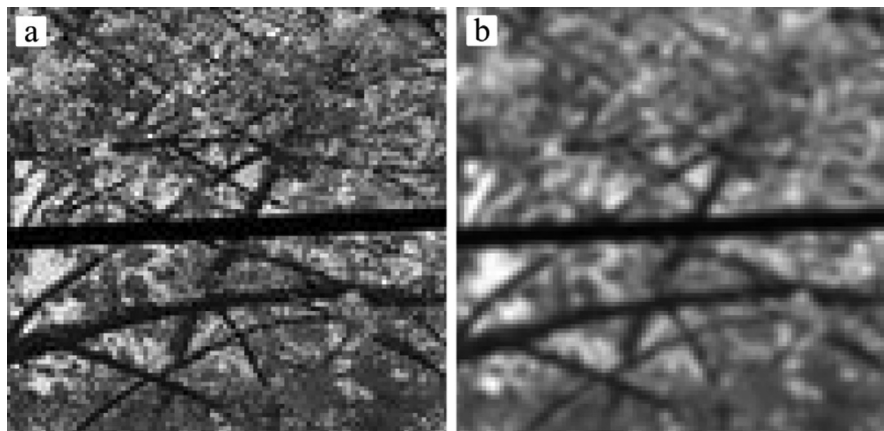

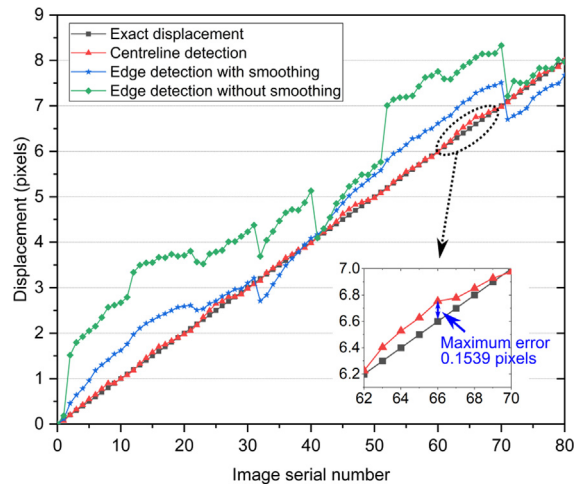**Fig. 14.** Smoothing effect. (a) before smoothing; (b) after smoothing.

Fig. 15. Accuracy comparison of the measured vertical displacement by the three subpixel detection methods.

rectangle in Fig. 13. Next, building the tracking window and the edge detection are performed in the same manner as in the edge detection without Gaussian smoothing, and the edge tracking point P_e (blue point) is obtained.

After all images are processed and the tracking points P_{track}, P_e and P'_e of the three subpixel detection methods are acquired separately, the vertical displacement of the contact wire can be obtained. Fig. 15 shows the measured vertical displacement of the contact wire for the three detection methods with the image serial number. The black line is the exact displacement, and the red, blue and green lines are the displacement results by the centreline detection method, the edge detection method with and without Gaussian smoothing, respectively. Table 1 shows the statistical analysis of the displacement error of these three different methods relative to the exact displacement. From Fig. 15 and Table 1, it can be concluded that the centreline detection has the better accuracy and robustness in this numerical experiment, and the measured displacement data of the centreline detection fluctuates only slightly around the exact displacement, which shows the stability of this method.

In Fig. 15 and Table 1, the edge detection with Gaussian smoothing (blue line) and without smoothing (green line) are compared to determine how much the Gaussian smoothing improves the accuracy of edge detection. We can obtain from Fig. 15 that the displacement result of the edge detection without smoothing is more volatile and unstable and is susceptible to environmental changes, leading the tracking data to oscillate substantially. By comparing their mean values and standard deviations of the displacement error, it can be concluded that the accuracy and stability of edge detection without smoothing is much worse than that with smoothing. Thus, a proper smoothing has a favourable influence on the accuracy of edge detection, and we suggest using smoothing for edge detection, especially in noisy environments.

4.2. Effect of diameter change of contact wire on tracking accuracy

The minimum recognizable diameter of the contact wire in the image is tested, and the effect of the diameter change of the contact wire, related to measurement distance, on tracking accuracy is studied. According to the pinhole camera model introduced in [26], the 12-mm diameter of the contact wire was approximately 22.909 to 2.864 pixels in the image with a lens focal length of 105 mm and the horizontal distance changing from 10 to 80 m, as shown in Table 2. Thus, the diameter increased from 3 to 23, with a total of 21 groups. Similar to the first numerical experiment, the black line with different diameters was used as the contact wire in the above background image. To test the robustness of the proposed algorithm, the contact wire was randomly distributed in the image and then moved by the same displacement of 50 pixels. Three detection methods tracked the contact wire, and the displacement error was obtained by comparing the displacement data with 50 pixels. This process was carried out 10 times, and 10 random positions are the same for each diameter group. The mean and standard deviation of the displacement error of each group are shown in Fig. 16.

In Fig. 16, the error bars show the means and standard deviations of the displacement error of three subpixel detection methods. The midpoint is the mean, and the upper and lower caps present the standard deviation of the displacement error. The mean result shows that the displacement error of the centreline detection and edge detection with Gaussian smoothing remains low, but the displacement error of edge detection without Gaussian smoothing is relatively higher. The reason is that smoothing can reduce the negative impact of the background noise on the accuracy of edge detection, so without Gaussian smoothing, the tracking accuracy of the edge detection method is reduced, and the displacement data become more unstable. These results demonstrate that smoothing is helpful to improve the accuracy and robustness of the edge detection method. Through a comparison of the standard deviation, the standard deviation of the centreline detection method always remains low, and far less than the standard deviation of the other two methods.

Table 1
Displacement error analysis of the three subpixel detection methods compared with the exact displacement.

	Mean (pixels)	Standard deviation (pixels)	Maximum value (pixels)	Minimum value (pixels)
Centreline detection	0.0456	0.0382	0.1539	0.0000
Edge detection with smoothing	0.4372	0.2235	0.8123	0.0128
Edge detection without smoothing	1.1494	0.6379	2.1961	0.0077

Table 2
The diameter of the contact wire at different horizontal measurement distances.

Distance (m)	10	20	30	40	50	60	70	80
Diameter (pixels)	22.909	11.455	7.636	5.727	4.582	3.818	3.273	2.864
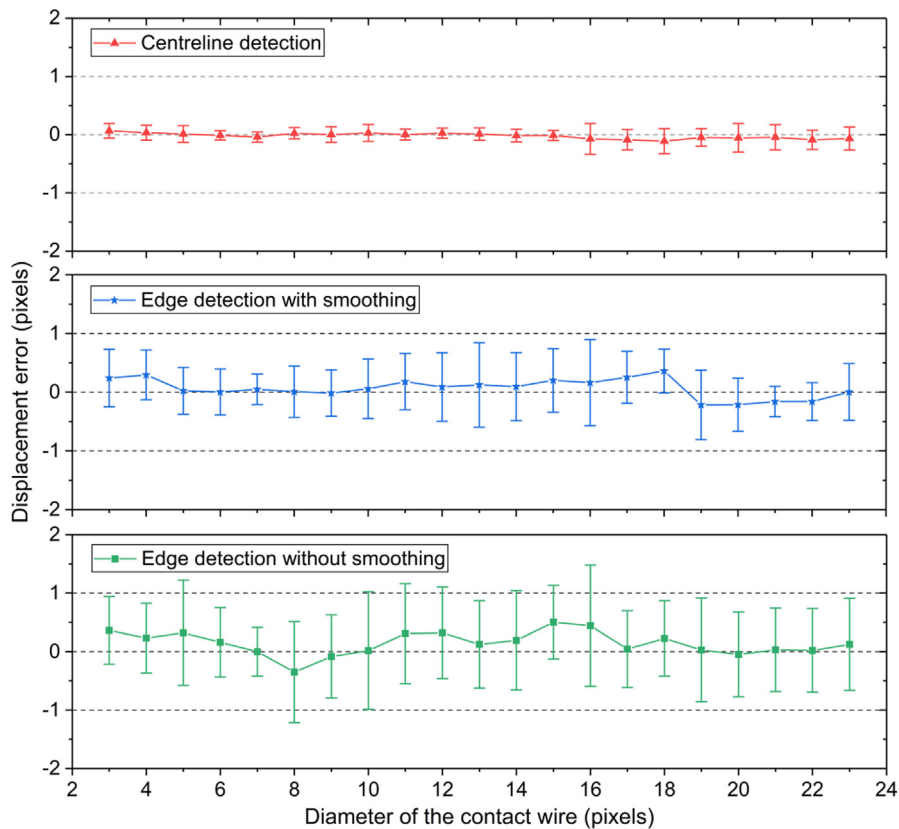
Fig. 16. Means and standard deviations of the displacement error of three subpixel detection methods.

The results also show that the three detection methods can successfully detect a minimum diameter of 3 pixels, which is sufficient to meet the regular uplift measurement of the catenary wire, with a measuring distance of less than 30 m and a minimum diameter of 8 pixels. The lower diameter, i.e., 1 or 2 pixels, has been tested, but it is challenging for the algorithm to detect. A longer telephoto lens can also be used to increase the effective measurement distance. The long measurement distance makes remote measurement relatively convenient and applicable, but it should be mentioned that the data instability caused by ultralong distance measurement needs to be noted. In the actual field measurement, a greater measurement distance would be more affected by atmospheric effects, light or other environmental conditions. Through a comparison of the effects of the diameter change on the accuracy, it can be concluded that the diameter change slightly affects the accuracy of the three subpixel detection methods in the case of a noisy background.
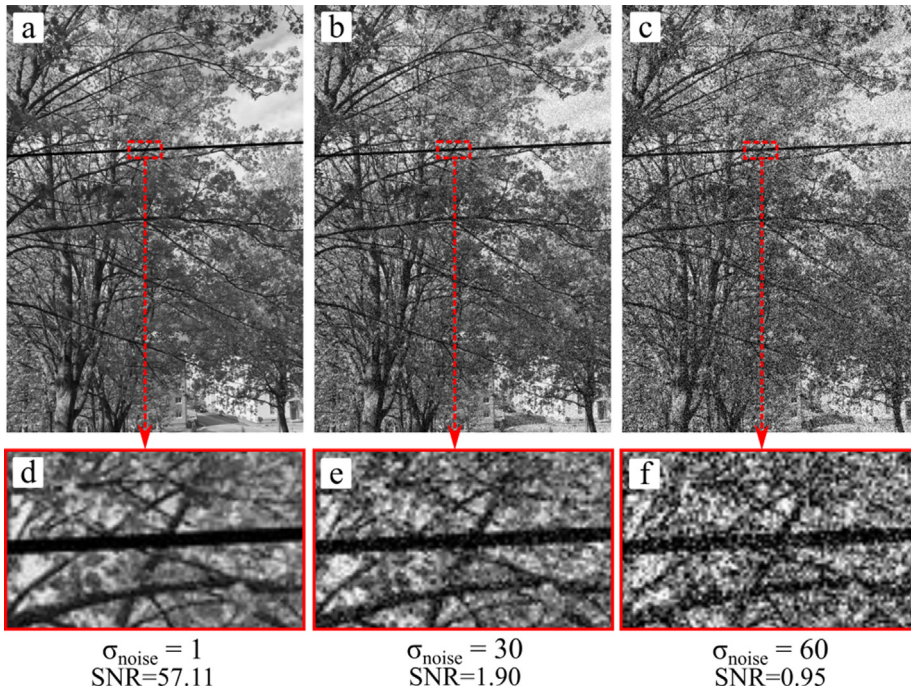
Fig. 17. Adding different degrees of Gaussian noise to the image. (a), (d) σ_{noise} = 1, SNR = 57.11; (b), (e) σ_{noise} = 30, SNR = 1.90; (c), (f) σ_{noise} = 60, SNR = 0.95.

4.3. Noise sensitivity

The robustness is very important for the tracking method during engineering applications, and the addition of Gaussian noise to the image was used to test the robustness of the tracking method. Different degree of Gaussian noise was added to the image by increasing the standard deviation σ_{noise} of the Gaussian function from 1 to 60 in increments of 5, with the contact wire remaining stationary, as shown in Fig. 17. Thus, there are 13 groups for different degrees of Gaussian noise, and every group generates 50 images of a random noise distribution. Fig. 17(d)–(f) show the local areas of (a), (b) and (c), respectively. With σ_{noise} increasing from 1 to 60, it can be seen that the number of noise points increases gradually and that the image, including the contact wire, is increasingly blurred. Especially for σ_{noise} = 60, there are many noise points on the contact wire, and the difference between the contact wire and tree branches in the background is tiny. Thus, the edge of the contact wire is harder to identify than that for σ_{noise} = 1.

Then, the three subpixel detection methods were used to identify the position of the contact wire, and the detection error was obtained by comparing the position results with the original position (σ_{noise} = 0). The signal-to-noise ratio (SNR) was
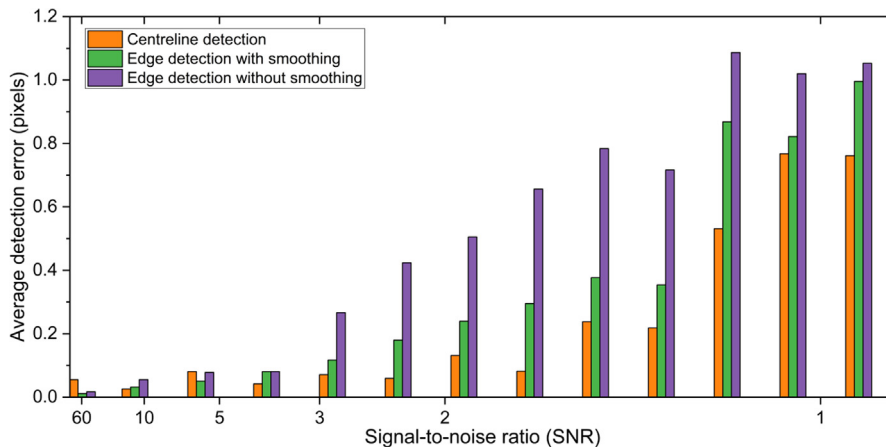

Fig. 18. Average detection errors of three detection methods under different degrees of Gaussian noise.
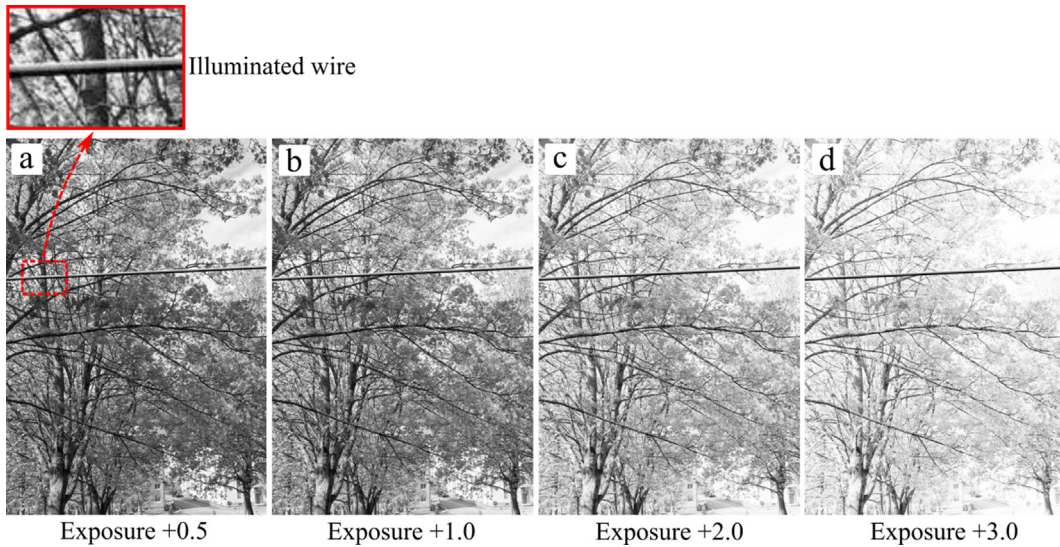
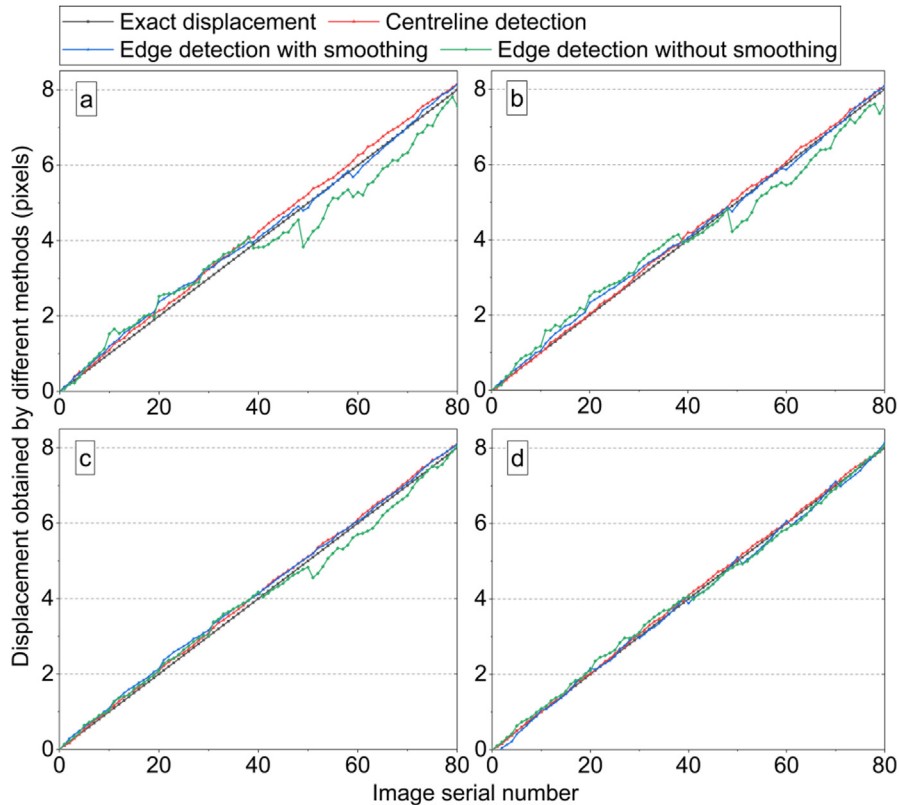**Fig. 19.** Simulation of different ambient light intensities.

Fig. 20. Accuracy comparison under different ambient light intensities. (a) exposure + 0.5; (b) exposure + 1.0; (c) exposure + 2.0; (d) exposure + 3.0.

used to estimate image noise in the imaging system. A higher SNR value means that the image quality is better. There are several image-based SNR definitions, and a simple SNR definition [46] is:

$$SNR = \frac{\sigma_{image}}{\sigma_{noise}}$$

(9)

where σ_{image} is the standard deviation of the intensity value of the original image, and σ_{noise} is the standard deviation of the added Gaussian noise. Thus, as the standard deviation σ_{noise} of the Gaussian noise increases from 1 to 60, the SNR decreases

from 57.11 to 0.95, and the image quality becomes lower. The average detection errors of 13 groups with the change of SNR is shown in Fig. 18.

As shown in Fig. 18, when the SNR is less than 3, the average detection error of the two edge detection methods begins to increase significantly. In contrast, the error of the centreline detection begins to increase significantly when the SNR is less than 1.5. In general, for the capacity to resist Gaussian noise, the centreline detection and edge detection with Gaussian
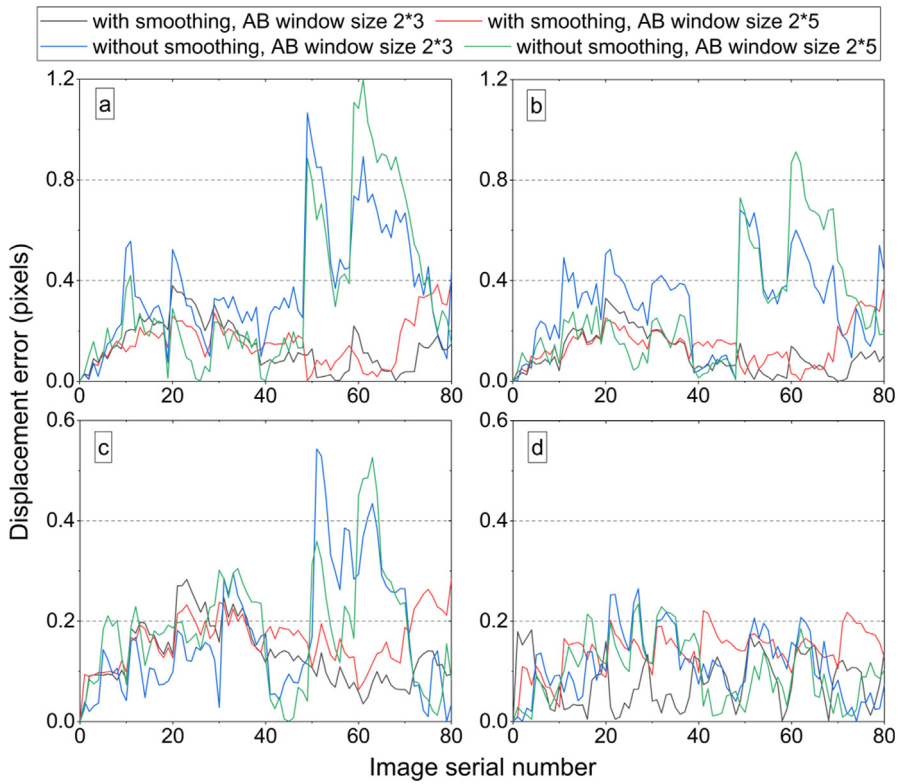

Fig. 21. The influence of different window sizes on the edge detection accuracy. (a) exposure + 0.5; (b) exposure + 1.0; (c) exposure + 2.0; (d) exposure + 3.0.
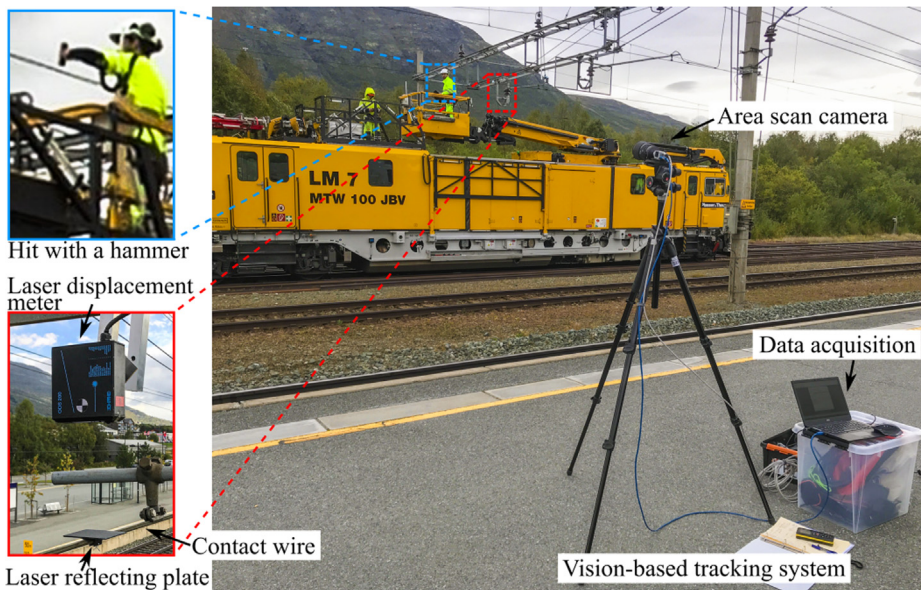

Fig. 22. Uplift measurement of a railway catenary system by the vision-based tracking system and the laser displacement meter. Photo: Tengjiao Jiang/ NTNU.
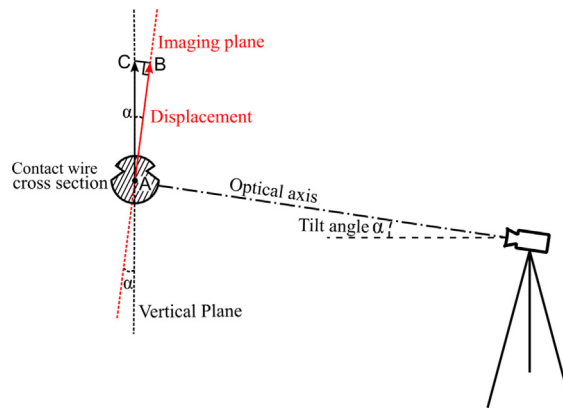
Fig. 23. The angle α between the imaging plane and the vertical plane.

smoothing are better than that of edge detection without Gaussian smoothing in this case. By comparing the two edge detection methods, it is shown that Gaussian smoothing is very useful for reducing the impact of noise, confirming edge detection to be relatively robust and accurate. When SNR = 0.95, centreline detection and edge detection can still reasonably accurately identify the contact wire, which shows the robustness of these two methods. In general, the real environment of the uplift measurement of the contact wire is much better than the condition SNR = 0.95. Thus, centreline detection and edge detection are competent for the most general conditions.

4.4. Different light intensities

Under different light intensities, the performances of the three subpixel detection methods are tested. An illuminated wire, under intense sunlight, is simulated by changing the intensity gradient from top to bottom, as shown in Fig. 19.

When the ambient light changes, the brightness of the background will also change. The light intensity of the background is simulated by adjusting the exposure compensation of a background image in an image processing software. The light intensity has been divided into four groups, exposure compensation +0.5, +1.0, +2.0 and +3.0, as shown in Fig. 19. The wire movement is similar to the numerical experiment in Section 4.1. The wire was moved downwards with a displacement inter-
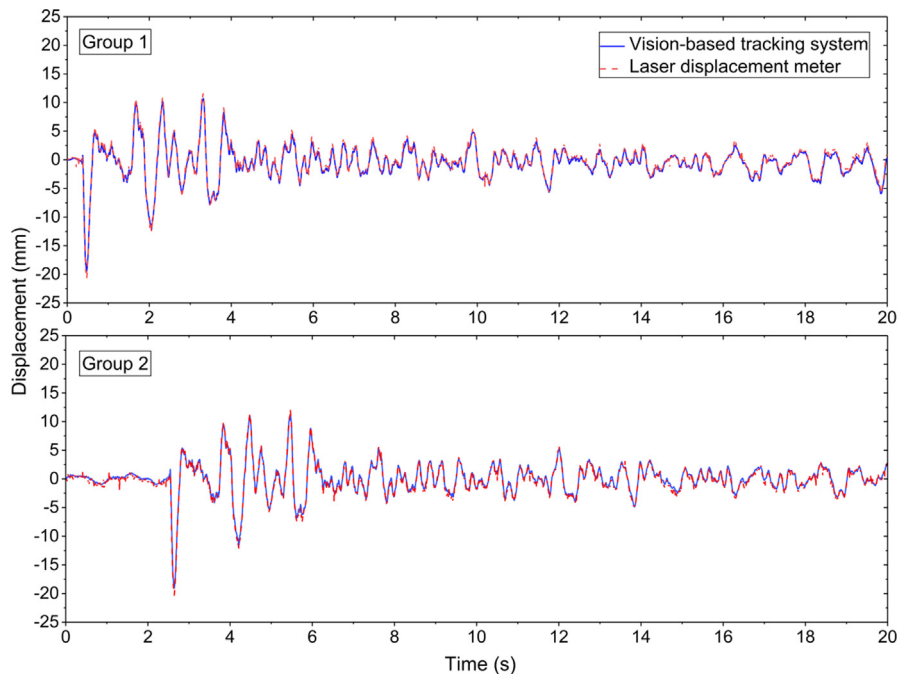

Fig. 24. Displacement obtained by the vision-based tracking system and the laser displacement meter.
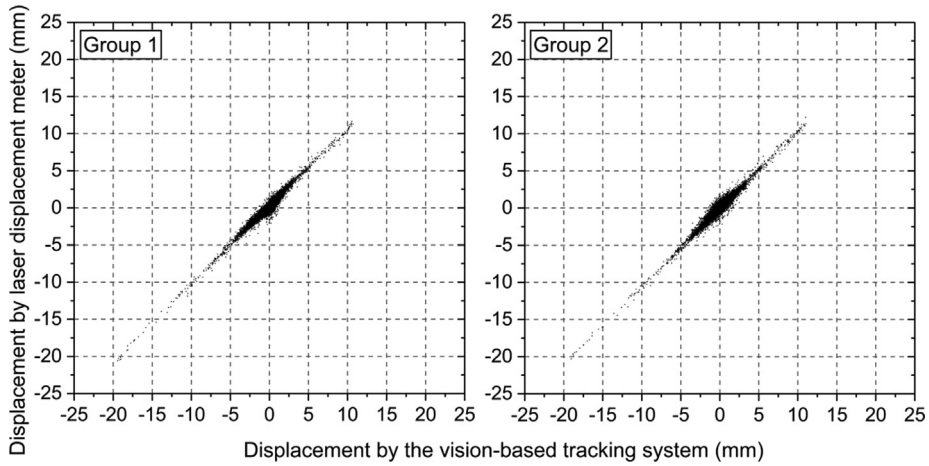
Fig. 25. Displacement comparison between the vision-based tracking system and the laser displacement meter.
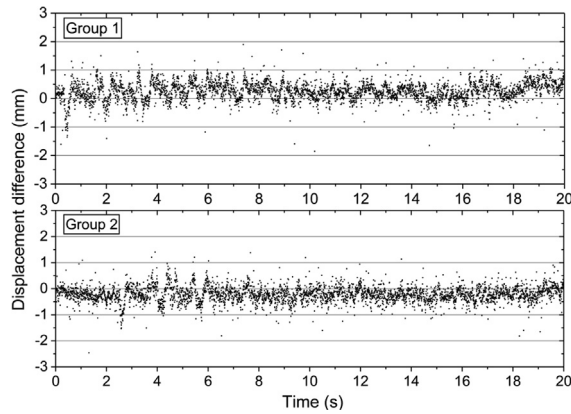

Fig. 26. Displacement differences between the vision-based tracking system and the laser displacement meter in time series.

val of 0.1 pixels, from 0 to 8.0 pixels, and a sequence of 81 images was generated and then processed separately by three different subpixel detection methods.

Fig. 20 is the displacement comparison results. The black line is the exact displacement, and the red, blue and green lines are the displacement results obtained by the centreline detection method and the edge detection method with and without Gaussian smoothing, respectively. Through the comparison, it can be found that the edge detection accuracy increases when the light intensity increases. The reason for this increase is that, as the light intensity of background increases, the intensity
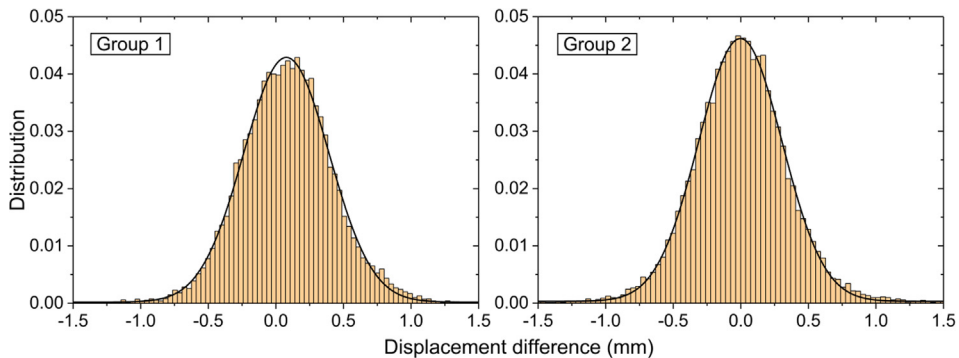

Fig. 27. Distributions of the displacement differences between the vision-based tracking system and the laser displacement meter.

difference between the wire and the background becomes larger. The significant intensity difference is beneficial to edge detection.

In some parts of Fig. 20, the accuracy of edge detection with Gaussian smoothing performs better than centreline detection, especially for the high light intensity. As mentioned above, the edge detection method is more suitable for the high light intensity situations because the lower edge has an obvious intensity gradient with the background and is easier to detect. This is why both methods have been introduced. Depending on the specific working situations, one of these two detection methods can be selected to increase the applicability of the proposed algorithm.

As mentioned in Section 3.2.2, one of the most critical factors affecting the accuracy of edge detection is the calculation of A and B, which are the average intensity values of the background and the contact wire, separately. Different window sizes will also affect the calculation of A and B. Therefore, under different light intensities, the influence of window sizes on the edge detection accuracy is tested.

Similarly, the light intensity is divided into four groups, and edge detection with and without smoothing methods are still used to detect the contact wire from the above 81 images. However, the different window sizes, i.e., 2 rows and 3 columns, 2 rows and 5 columns, are used for the edge detection methods, separately. Finally, the displacement results are compared with the exact displacement, and the displacement error results are obtained, as shown in Fig. 21. The large window is more susceptible to the background intensity change under the sharp luminosity gradients. For the exposure compensation + 3.0 group, the influence of the window sizes decreases, because the background is bright, and the intensity gradient of the background decreases. Therefore, it can be concluded that for the background with sharp luminosity gradients, the window size of 2 rows and 3 columns is recommended for the calculation of intensity values A and B.

5. Field application validation

5.1. Field uplift measurement of railway catenary systems

To test the performance of the proposed vision-based tracking system in an outdoor environment, a field uplift measurement of a railway catenary system was carried out. The accuracy of the vision-based tracking system is tested by comparing the vision-based tracking system with a laser displacement meter. In the field test, the vision-based tracking system was mounted at a distance from the railway and measurements were carried out without contact to the catenary system. The laser displacement meter (DME ODS200) was mounted on the support structure above the contact wire, and a laser reflecting plate was mounted on the contact wire to measure the uplift. A schematic overview of the field uplift measurement is shown in Fig. 22.

In this case, the contact wire was fixedly excited by an impulse model hammer, and then, the uplift data of the contact wire were obtained by these two devices simultaneously with the sampling frequency of 200 Hz. A medium telephoto lens (Sigma AF 105 mm f/2.8 Macro DG OS) was used with a focal length of 105 mm. The horizontal distance L_H between the contact wire and the camera was 7.65 m, and the tilt angle α was 25.35°, measured by the laser range finder. Through the image processing by the proposed line-tracking algorithm, the displacement of the contact wire (in pixels) is obtained. To compare

Pantograph-catenary system

Fig. 28. Trams with the pantograph-catenary system. Photo: Tengjiao Jiang/NTNU.

with the laser displacement meter, the displacement in pixels was converted to physical units in millimetres by using the pinhole camera calibration model, described in [26]. Due to the continuous movement of the contact wire throughout the whole image, the scaling factor from the pixel displacement to physical units is not constant and changes slightly. In this case, the scaling factor depends on various parameters, including the image coordinates of the tracking point, the tilt angle α of the camera, the focal length f of the camera lens, as well as the object distance L of the measurement point.

Due to the tilt angle α, the imaging plane usually does not coincide with the vertical plane, and there is also an angle α, as shown in Fig. 23. Because the angle α is small and the vibration of the contact wire is mainly in the vertical direction, the vertical displacement can be estimated as $AC = AB/\cos\alpha$. There is only a small error between the real vertical displacement and the estimated one, AC. AB is the displacement in the image plane. The tilt angle, 25.35°, is in the upper range that we can accept in the field measurement.

The accuracy of the laser is approximately 0.05 mm for the measuring range 10 to 30 cm and is considered to be ground truth for this application. Two groups of the displacement data obtained from these two devices are compared with each
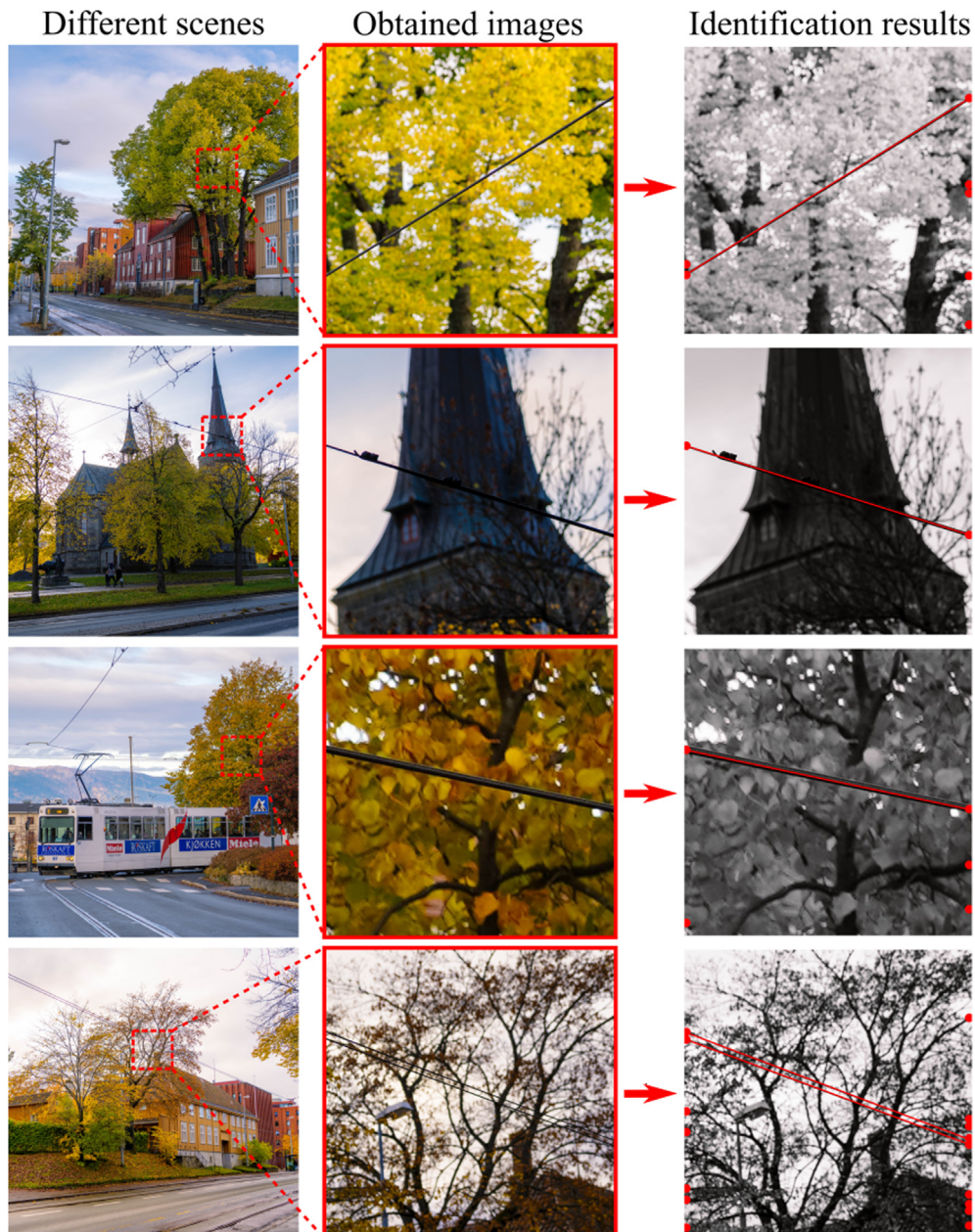

Fig. 29. Identification of contact wires. Photo: Tengjiao Jiang/NTNU.

other in a time series. Both groups obtained data for more than 80 seconds, and the comparison results of the first 20 seconds are shown in Fig. 24.

Fig. 25 shows that the two measurement methods correlate well, indicating that the accuracy of the tracking system is very close to the laser displacement meter. This is also confirmed by the displacement differences between the two measurement methods in time series, shown in Fig. 26, and the distributions of the displacement differences, shown in Fig. 27. Fig. 27 shows that a Gaussian distribution fits well with the data. The mean values of group 1 and 2 are 0.077 and −0.0036 mm, and the standard deviations are 0.32 and 0.31 mm, respectively. The accuracy of the proposed vision-based tracking system is ± 0. 6 mm at 95% confidence, with compensation for the tilt angle. From the application results, it can be concluded that the proposed vision-based tracking system, with the line-tracking method, can successfully and accurately measure the uplift of the railway catenary system.

5.2. Identifying the contact wire in a diverse city environment

This section demonstrates the ability of the proposed tracking algorithm to identify a contact wire in a diverse environment. Fig. 28 shows the Trondheim city tram and its pantograph-catenary system. The city environment provides challenging scenes for contact wire detection, as shown in the examples in the left column of Fig. 29. The middle column of Fig. 29 depicts obtained images at the contact wire location, and the right column shows the identification results of the contact wire with the algorithm. The right column images also show the candidate endpoints as red dots at the left and right boundaries and the identified contact wire as a red line. The images with many tree branches generally have the most candidate points, see, e.g., the bottom right image in Fig. 29. This is expected because these tree branches are similar to contact wires
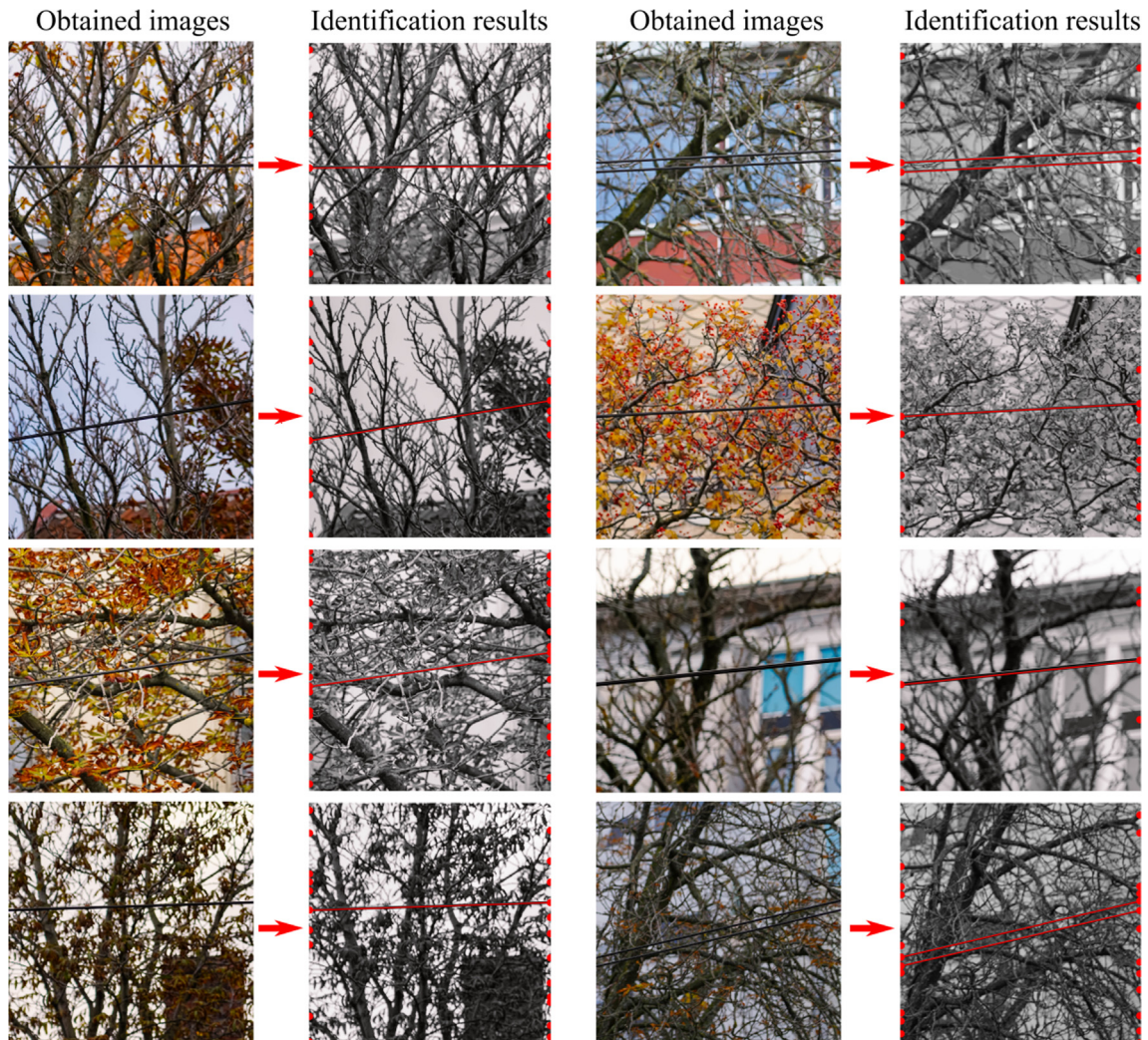

Fig. 30. Applications with more complex backgrounds. Photo: Tengjiao Jiang/NTNU.

and are correctly identified as candidate points. However, the line search ensures that the contact wires can be found in the noisy background. Fig. 29 shows that the contact wire is correctly identified in all example scenes.

After comparing different scenes, the background with tree branches is considered to be the most difficult case because it induces the largest number of candidate points. To test the robustness of the algorithm, more applications with different tree branches as backgrounds are carried out, as shown in Fig. 30. The resulting images show that the candidate points on both boundaries increase dramatically as tree branches are identified as possible contact wire endpoints. However, again, after line search, the algorithm has successfully identified the contact wires.

Through the identification of the contact wire in a diverse city environment, it can be concluded that the algorithm can deal with many different types of noisy backgrounds in diverse working conditions. In all applications with different noisy levels, the algorithm can successfully identify contact wires, which shows the robustness of the algorithm.

6. Conclusions

A portable vision-based tracking system is proposed to be applied for truly remote, non-contact and non-target uplift measurements of a catenary system. To address the general problem, which is that the contact wire is challenging to track without a target in front of a noisy background, a robust line-tracking technique based on a coarse subset and line search and subpixel detection is proposed to track linear objects in front of a noisy background. Components of the vision-based tracking system and principles of the line-tracking technique are described in detail. Subpixel detection includes two methods, centreline detection and edge detection. These two methods complement each other's application scope, and one of these two subpixel detection methods can be used according to different application environments to improve the applicability of the whole system.

The accuracy, robustness and applicability of the vision-based tracking system are demonstrated through numerical experiments, the field uplift measurement of the railway catenary system and the identification of the contact wire in a diverse city environment. From the obtained results, it can be concluded that the proposed line-tracking method can successfully track the contact wire in front of a noisy background.

CRediT authorship contribution statement

Tengjiao Jiang: Conceptualization, Methodology, Software, Investigation, Writing - review & editing. **Gunnstein Thomas Frøseth:** Conceptualization, Methodology, Software, Investigation, Writing - review & editing. **Anders Rønnquist:** Conceptualization, Methodology, Software, Investigation, Writing - review & editing. **Egil Fagerholt:** Conceptualization, Methodology, Software, Investigation, Writing - review & editing.

Declaration of Competing Interest

The authors declare that they have no known competing financial interests or personal relationships that could have appeared to influence the work reported in this paper.

Acknowledgements

References

[1] X. Hong, J. Zhou, Y. He, Damage detection of anchored region on the messenger cable based on matching pursuit algorithm, Mech. Syst. Signal Process. 130 (2019) 221–247, https://doi.org/10.1016/j.ymssp.2019.04.053.

[2] S. Huang, Y. Zhai, M. Zhang, X. Hou, Arc detection and recognition in pantograph–catenary system based on convolutional neural network, Inf. Sci. 501 (2019) 363–376, https://doi.org/10.1016/j.ins.2019.06.006.

[3] D. Zhang, S. Gao, L. Yu, G. Kang, D. Zhan, X. Wei, A Robust Pantograph-Catenary Interaction Condition Monitoring Method Based on Deep Convolutional Network, IEEE Transactions on Instrumentation and Measurement (2019) 1-1. https://doi.org/10.1109/TIM.2019.2920721.

[4] M. Tan, N. Zhou, J. Wang, D. Zou, W. Zhang, G. Mei, A real-time impact detection and diagnosis system of catenary using measured strains by fibre Bragg grating sensors, Veh. Syst. Dyn. 57 (2019) 1924–1946, https://doi.org/10.1080/00423114.2018.1556396.

[5] J. Ambrósio, J. Pombo, M. Pereira, P. Antunes, A. Mósca, Recent developments in pantograph-catenary interaction modelling and analysis, Int. J. Railw. Technol. 1 (2012) 249–278, https://doi.org/10.4203/ijrt.1.1.12.

[6] Z. Liu, Detection and Estimation Research of High-speed Railway Catenary, Springer, Singapore, 2017.

[7] M. Bocciolone, G. Bucca, A. Collina, L. Comolli, Pantograph–catenary monitoring by means of fibre Bragg grating sensors: Results from tests in an underground line, Mech. Syst. Signal Process. 41 (2013) 226–238, https://doi.org/10.1016/j.ymssp.2013.06.030.

[8] Y. Park, Y.-H. Cho, K. Lee, H.-J. Kim, I.-C. Kim, Development of an Uplift Measurement System for Overhead Contact Wire using High Speed Camera, J. Korean Inst. Electr. Electron. Mater. Eng. 22 (2009) 864–869, https://doi.org/10.4313/JKEM.2009.22.10.864.

[9] G. Laffont, N. Roussel, S. Rougeault, J. Boussoir, L. Maurin, P. Ferdinand, Innovative FBG sensing techniques for the railway industry: Application to overhead contact line monitoring, in: Proceedings of SPIE - 20th International Conference on Optical Fibre Sensors, SPIE, Edinburgh, United Kingdom, 2009, pp. 1–4.

[10] C.A.L. Vázquez, M.M. Quintas, M.M. Romera, Non-contact sensor for monitoring catenary-pantograph interaction, in: 2010 IEEE International Symposium on Industrial Electronics, IEEE, Bari, Italy, 2010, pp. 482–487.

[11] K. Karwowski, M. Mizan, D. Karkosinski, Monitoring of current collectors on the railway line, Transport 33 (2016) 177–185, https://doi.org/10.3846/16484142.2016.1144222.

[12] P. Nåvik, A. Rønnquist, S. Stichel, Identification of system damping in railway catenary wire systems from full-scale measurements, Eng. Struct. 113 (2016) 71–78, https://doi.org/10.1016/j.engstruct.2016.01.031.

[13] P. Nåvik, A. Rønnquist, S. Stichel, A wireless railway catenary structural monitoring system: Full-scale case study, Case Stud. Struct. Eng. 6 (2016) 22–30, https://doi.org/10.1016/j.csse.2016.05.003.

[14] C. Rainieri, G. Fabbrocino, Operational Modal Analysis of Civil Engineering Structures, Springer, New York, NY, 2014.

[15] D. Zou, N. Zhou, L. Rui Ping, G.M. Mei, W.H. Zhang, Experimental and simulation study of wave motion upon railway overhead wire systems, Proc. Inst. Mech. Eng. Part F: J. Rail Rapid Transit 231 (2017) 934–944, https://doi.org/10.1177/0954409716648718.

[16] D. Zou, W.H. Zhang, R.P. Li, N. Zhou, G.M. Mei, Determining damping characteristics of railway-overhead-wire system for finite-element analysis, Veh. Syst. Dyn. 54 (2016) 902–917, https://doi.org/10.1080/00423114.2016.1172715.

[17] G. Frøseth, P. Nåvik, A. Rønnquist, Operational displacement estimations of railway catenary systems by photogrammetry and the integration of acceleration time series, Int. J. Railw. Technol. (2019) (accepted for publication).

[18] H.A. Bruck, S.R. McNeill, M.A. Sutton, W.H. Peters, Digital image correlation using Newton-Raphson method of partial differential correction, Exp. Mech. 29 (1989) 261–267, https://doi.org/10.1007/BF02321405.

[19] B. Pan, K. Li, W. Tong, Fast, robust and accurate digital image correlation calculation without redundant computations, Exp. Mech. 53 (2013) 1277–1289, https://doi.org/10.1007/s11340-013-9717-6.

[20] B. Pan, K. Li, A fast digital image correlation method for deformation measurement, Opt. Lasers Eng. 49 (2011) 841–847, https://doi.org/10.1016/j.optlaseng.2011.02.023.

[21] M. Bornert, F. Brémand, P. Doumalin, J.C. Dupré, M. Fazzini, M. Grédiac, F. Hild, S. Mistou, J. Molimard, J.J. Orteu, L. Robert, Y. Surrel, P. Vacher, B. Wattrisse, Assessment of digital image correlation measurement errors: methodology and results, Exp. Mech. 49 (2009) 353–370, https://doi.org/10.1007/s11340-008-9204-7.

[22] B. Pan, K. Qian, H. Xie, A. Asundi, Two-dimensional digital image correlation for in-plane displacement and strain measurement: a review, Meas. Sci. Technol. 20 (2009), https://doi.org/10.1088/0957-0233/20/6/062001 062001.

[23] L. Yu, B. Pan, Single-camera high-speed stereo-digital image correlation for full-field vibration measurement, Mech. Syst. Signal Process. 94 (2017) 374–383, https://doi.org/10.1016/j.ymssp.2017.03.008.

[24] D.L.B.R. Jurjo, C. Magluta, N. Roitman, P. Batista, Gonçalves, Analysis of the structural behavior of a membrane using digital image processing, Mech. Syst. Signal Process. 54–55 (2015) 394–404, https://doi.org/10.1016/j.ymssp.2014.08.010.

[25] J. Soons, P. Lava, D. Debruyne, J. Dirckx, Full-field optical deformation measurement in biomechanics: Digital speckle pattern interferometry and 3D digital image correlation applied to bird beaks, J. Mech. Behav. Biomed. Mater. 14 (2012) 186–191, https://doi.org/10.1016/j.jmbbm.2012.05.004.

[26] B. Pan, L. Tian, X. Song, Real-time, non-contact and targetless measurement of vertical deflection of bridges using off-axis digital image correlation, NDT E Int. 79 (2016) 73–80, https://doi.org/10.1016/j.ndteint.2015.12.006.

[27] S.-W. Kim, N.-S. Kim, Dynamic characteristics of suspension bridge hanger cables using digital image processing, NDT E Int. 59 (2013) 25–33, https://doi.org/10.1016/j.ndteint.2013.05.002.

[28] J.-E. Dufour, B. Beaubier, F. Hild, S. Roux, CAD-based Displacement Measurements with Stereo-DIC, Exp. Mech. 55 (2015) 1657–1668, https://doi.org/10.1007/s11340-015-0065-6.

[29] C. Warren, C. Niezrecki, P. Avitabile, P. Pingle, Comparison of FRF measurements and mode shapes determined using optically image based, laser, and accelerometer measurements, Mech. Syst. Signal Process. 25 (2011) 2191–2202, https://doi.org/10.1016/j.ymssp.2011.01.018.

[30] F. Hild, S. Roux, Digital image correlation: from displacement measurement to identification of elastic properties – a review, Strain 42 (2006) 69–80, https://doi.org/10.1111/j.1475-1305.2006.00258.x.

[31] L. Felipe-Sesé, F.A. Díaz, Damage methodology approach on a composite panel based on a combination of fringe projection and 2D digital image correlation, Mech. Syst. Signal Process. 101 (2018) 467–479, https://doi.org/10.1016/j.ymssp.2017.09.002.

[32] P. Poozesh, J. Baqersad, C. Niezrecki, P. Avitabile, E. Harvey, R. Yarala, Large-area photogrammetry based testing of wind turbine blades, Mech. Syst. Signal Process. 86 (2017) 98–115, https://doi.org/10.1016/j.ymssp.2016.07.021.

[33] R. Huňady, M. Hagara, A new procedure of modal parameter estimation for high-speed digital image correlation, Mech. Syst. Signal Process. 93 (2017) 66–79, https://doi.org/10.1016/j.ymssp.2017.02.010.

[34] L. Huynh, J. Rotella, M.D. Sangid, Fatigue behavior of IN718 microtrusses produced via additive manufacturing, Mater. Des. 105 (2016) 278–289, https://doi.org/10.1016/j.matdes.2016.05.032.

[35] A.S. Wu, D.W. Brown, M. Kumar, G.F. Gallegos, W.E. King, An experimental investigation into additive manufacturing-induced residual stresses in 316L stainless steel, Metall. Mater. Trans. A 45 (2014) 6260–6270, https://doi.org/10.1007/s11661-014-2549-x.

[36] P. Chowdhury, H. Sehitoglu, R. Rateick, Damage tolerance of carbon-carbon composites in aerospace application, Carbon 126 (2018) 382–393, https://doi.org/10.1016/j.carbon.2017.10.019.

[37] M. Flores, D. Mollenhauer, V. Runatunga, T. Beberniss, D. Rapking, M. Pankow, High-speed 3D digital image correlation of low-velocity impacts on composite plates, Compos. Part B: Eng. 131 (2017) 153–164, https://doi.org/10.1016/j.compositesb.2017.07.078.

[38] Y. Du, F.A. Diaz, R.L. Burguete, E.A. Patterson, Evaluation using digital image correlation of stress intensity factors in an aerospace panel, Exp. Mech. 51 (2011) 45–57, https://doi.org/10.1007/s11340-010-9335-5.

[39] A. Borkar, M. Hayes, M.T. Smith, Robust lane detection and tracking with ransac and Kalman filter, in: 2009 16th IEEE International Conference on Image Processing (ICIP), IEEE, Cairo, Egypt, 2009, pp. 3261-3264.

[40] H.-C. Kuo, L.-J. Wu, An image tracking system for welded seams using fuzzy logic, J. Mater. Process. Technol. 120 (2002) 169–185, https://doi.org/10.1016/S0924-0136(01)01155-4.

[41] Z. Li, Y. Liu, R. Walker, R. Hayward, J. Zhang, Towards automatic power line detection for a UAV surveillance system using pulse coupled neural filter and an improved Hough transform, Mach. Vis. Appl. 21 (2010) 677–686, https://doi.org/10.1007/s00138-009-0206-y.

[42] I. Golightly, D. Jones, Corner detection and matching for visual tracking during power line inspection, Image Vis. Comput. 21 (2003) 827–840, https://doi.org/10.1016/S0262-8856(03)00097-0.

[43] R.O. Duda, P.E. Hart, Use of the Hough Transform to Detect Lines and Curves in Pictures, Commun. ACM 15 (1972) 11–15, https://doi.org/10.1145/361237.361242.

[44] A. Trujillo-Pino, K. Krissian, M. Alemán-Flores, D. Santana-Cedrés, Accurate subpixel edge location based on partial area effect, Image Vis. Comput. 31 (2013) 72–90, https://doi.org/10.1016/j.imavis.2012.10.005.

[45] J. Javh, J. Slavič, M. Boltežar, The subpixel resolution of optical-flow-based modal analysis, Mech. Syst. Signal Process. 88 (2017) 89–99, https://doi.org/10.1016/j.ymssp.2016.11.009.

[46] P.M. Atkinson, I.M. Sargent, G.M. Foody, J. Williams, Exploring the Geostatistical Method for Estimating the Signal-to-Noise Ratio of Images, Photogramm. Eng. Remote Sensing 73 (2007) 841–850, https://doi.org/10.14358/PERS.73.7.841.

[47] Tengjiao Jiang, Gunnstein Thomas Frøseth, Anders Rønnquist, Egil Fagerholt, A Vision-Based Line-Tracking Technique, Zenodo, 2020, Version 1.1. https://doi.org/10.5281/zenodo.3685219.